

# 4D large scale variational data assimilation of a turbulent flow with a dynamics error model

Pranav Chandramouli, Etienne Mémin, Dominique Heitz

## ► To cite this version:

Pranav Chandramouli, Etienne Mémin, Dominique Heitz. 4D large scale variational data assimilation of a turbulent flow with a dynamics error model. *Journal of Computational Physics*, Elsevier, 2020, 412, 10.1016/j.jcp.2020.109446 . hal-02547763

**HAL Id: hal-02547763**

**<https://hal.inria.fr/hal-02547763>**

Submitted on 20 Apr 2020

**HAL** is a multi-disciplinary open access archive for the deposit and dissemination of scientific research documents, whether they are published or not. The documents may come from teaching and research institutions in France or abroad, or from public or private research centers.

L'archive ouverte pluridisciplinaire **HAL**, est destinée au dépôt et à la diffusion de documents scientifiques de niveau recherche, publiés ou non, émanant des établissements d'enseignement et de recherche français ou étrangers, des laboratoires publics ou privés.

# 4D large scale variational data assimilation of a turbulent flow with a dynamics error model

Pranav Chandramouli<sup>1</sup>, Etienne Memin

*Fluminance - INRIA, 263 Avenue General Leclerc, Rennes*

Dominique Heitz

*Irstea, UR OPAALE, F-35044 Rennes Cedex, France*

---

## Abstract

We present a variational assimilation technique (4D-Var) to reconstruct time resolved incompressible turbulent flows from measurements on two orthogonal 2D planes. The proposed technique incorporates an error term associated to the flow dynamics. It is therefore a compromise between a strong constraint assimilation procedure (for which the dynamical model is assumed to be perfectly known) and a weak constraint variational assimilation which considers a model enriched by an additive Gaussian forcing. The first solution would require either an unaffordable direct numerical simulation (DNS) of the model at the finest scale or an inaccurate and numerically unstable large scale simulation without parametrisation of the unresolved scales. The second option, the weakly constrained assimilation, relies on a blind error model that needs to be estimated from the data. This latter option is also computationally impractical for turbulent flow models as it requires to augment the state variable by an error variable of the same dimension. The proposed 4D-Var algorithm is successfully applied on a 3D turbulent wake flow in the transitional regime without specifying the obstacle geometry. The algorithm is validated on a synthetic 3D data-set with full-scale information. The performance of the algorithm is further analysed on data emulating large-scale experimental PIV observations.

---

<sup>1</sup>Corresponding author; Email: pranav.chandramouli@inria.fr

*Keywords:* 4D variation assimilation, turbulent wake flow,  
adjoint-optimisation, stochastic flow dynamics, dynamics error model

---

## 1. Introduction

Computational fluid dynamics (CFD) and experimental fluid dynamics (EFD) represent two established yet limited sets of techniques for the study of fluid flows. Both family of methods provides distinct advantages in representing and  
5 studying fluid flows. Similarly, they are both restricted in application by certain limitations. These limitations display a complementarity between the two fields. CFD is limited by the accuracy of its inlet and initial conditions, while EFD is capable of measuring an accurate initial and inlet conditions. The latter is limited in spatial extent while a large domain can be simulated using the former.  
10 EFD is capable of measuring accurate but sparse and selective flow field properties while CFD is capable of measuring an approximate but complete flow-field properties over a large domain. The exploitation of this complementarity by using a dynamical model guided by experimental observations is termed as data assimilation (DA).

15 DA, as a field, has been mainly driven by the works of researchers from the atmospheric and oceanographic sciences. The existing set of DA procedures can be broadly categorised into two main categories. Methods which are derived from stochastic filtering principles fall under the category of sequential data assimilation (SDA) approaches. The particle filter method [19], the Ensemble  
20 Kalman Filter (EnKF) [13], or a combination of both methods [33] are prominent examples of this method. These Monte Carlo methods are generally based on the principle of Bayesian minimum variance estimation. They are termed as ‘sequential’ due to the constant forward propagation of the system state statistics. Observations are assimilated to correct the predicted state when  
25 measurements are available along the state trajectory.

The second category of DA procedures are referred to as variational data assimilation (VDA) approaches and these originate from concepts of optimal con-

trol theory and variation calculus thus deriving the name [27]. These methods aim to estimate the optimal trajectory, starting from a background condition, which minimises a cost function leading to lowest error between system and observations. The works of Bergthórsson and Döös [2], Cressman [10] on optimal interpolation methods were stepping stones to the VDA methods. With VDA, the approaches can be classified into 3D variational and 4D variational methods depending on the spatial dimensions of the simulation and the inclusion, or not, of a temporal window for the system’s dynamical evolution. A first application of such methods was done by Sasaki [38] who further extended them to 4D analysis in Sasaki [39]. Since then, variants of the VDA approach have been used for DA with Le Dimet and Talagrand [26] being the prominent seminal reference for large scale data driven forecasting issues related to geophysical fluids.

Both categories of DA methods require significant computational power in order to provide meaningful results. This has constrained the application of DA to simple 2D flows in fluid mechanics such as the works of Mons et al. [30, 31]. In the context of SDA methods, Meldi and Poux [28] proposed a Kalman filter based assimilation technique for the reconstruction of 3D, unsteady turbulent flows using a reduced order model for cost-reduction. The successful application of the method portrayed the capability of DA methods despite the sub-optimality of Kalman filters in a nonlinear context. Astutely, a reduced order expression of the error covariance matrix, is introduced and aims at the same state-space reduction objective as those achieved by ensemble Kalman procedures (EnKF) [14]. However, contrary to those Monte-Carlo filters the nonlinearity of the dynamics is not fully taken into account. Furthermore, the turbulent “error” model is not optimised through the assimilation. Given the varied strengths of the two DA methods, VDA is better suited for state estimation while SDA has been the optimal choice for parameter estimation. This is because VDA takes into account future observations for state estimation while SDA corrects the current state of the system based only on current and past observations. On the other hand, it is easier to perform parameter optimisation in SDA as in VDA parameter optimisation requires the adjoint of the



dynamical model with respect to the parameter. However, this was observed to  
60 be challenging to perform even using SDA unless in a reduced-order sense by  
[43].

This work is a first attempt, to the extent of the Authors' knowledge, at  
simulating 3D, unsteady turbulent flows using principles of VDA from an exper-  
imentally realisable set of PIV data. The VDA approach developed by Grons-  
65 et al. [20] for 2D DNS of cylinder wake flow forms a basis for this work. A  
similar adjoint-based approach using PTV data was done by [40] for a planar  
jet. The ideal 4D assimilation with a perfect dynamical model would require  
an impractical DNS which is clearly unaffordable. In the proposed method, the  
computational cost reduction is achieved by coupling a recently proposed flow  
70 model, arising from a stochastic analysis of error propagation, termed modelling  
under location uncertainty (LU) by Mémin [29] (described in §3) with the as-  
similation algorithm. This strategy enables a significant reduction in the resolu-  
tion required for the simulation and provides a meaningful error or “turbulence”  
model associated to the unresolved component of the flow. In addition, such  
75 a coupling provides an opportunity to tune the contribution of the model by  
introducing it as a control parameter in the optimisation procedure. Thus, the  
methodology used for cost-reduction, which tends to introduce errors, is itself  
corrected by the assimilation algorithm. The ability to locally optimise model  
contribution is an important research question in the field of DA - this is ex-  
80 plored in § 5. This technique enables an alternative solution to the blind weakly  
constrained assimilation technique in which an error variable is added to the  
unknown state variable (namely the velocity and pressure). In such weakly con-  
strained system, the error variable is generally modelled as an additive forcing  
variable varying in space and time – and thus of the same dimension as the state  
85 variable. The corresponding control problem, which requires the estimation of  
an initial condition, an inlet and/or outlet condition and a full trajectory of  
an error variable related to the unresolved small scales, is computationally very  
expensive. Such a solution is in practice restricted to the assimilation of reduced  
order models [1, 11]. Contrary to this unaffordable solution, the technique we

90 propose, relies on the estimation of a stationary spatially varying coefficient of an adapted error model that accounts for unresolved turbulent scales of motion.

The principles of VDA and the adjoint-based optimisation procedure is enumerated in §2. The formulation of the LU model and its numerical treatment for VDA is presented in §3. The resultant code, termed as 4D-Var, is capable of performing VDA on flows of higher Reynolds numbers that were previously limited  
95 by high computational cost. This 4D-Var approach is used to optimise a three dimensional three component (3D3C) velocity field for wake flow at  $Re = 3900$  while assimilating time-resolved observations in §4. The possibility to tune the error model by introducing the model coefficient as a control parameter in the  
100 optimisation algorithm is explored in §5. A final section of concluding remarks follows.

## 2. Variational data assimilation

### 2.1. Mathematical representation:

DA techniques have a dual objective: to improve knowledge of the current system trajectory ( $\mathcal{X}_t$ ) (also called the analysis trajectory) based on observations ( $\mathcal{Y}_t$ ) and an *a priori* known background condition ( $\mathcal{X}^b$ ), and to predict an accurate future state of the system from current and past observations. Mathematically it can be expressed as:

$$\partial_t \mathcal{X}_t(\mathbf{x}) + \mathbb{M}(\mathcal{X}_t(\mathbf{x})) = \mathbf{q}_t, \quad (1)$$

$$\mathcal{X}_0(\mathbf{x}) = \mathcal{X}_0^b(\mathbf{x}) + \boldsymbol{\eta}, \quad (2)$$

$$\mathcal{Y}_t = \mathbb{H}(\mathcal{X}_t(\mathbf{x})) + \boldsymbol{\epsilon}_t, \quad (3)$$

where the state space trajectory  $\mathcal{X}_t$  is provided through the integration of a dynamical evolution model  $\mathbb{M}$  of the system from an initial condition *a priori*  
105 known only up to a noisy background state  $\mathcal{X}_0^b$  and, from a sparse set of noisy observations  $\mathcal{Y}$ . The sub-script denotes the temporal state of the system, and the super-script denotes the type of system state, i.e. background (*b*).

The noise attached to the dynamics, the initial condition and the observations  
 110 (respectively  $\mathbf{q}$ ,  $\boldsymbol{\eta}$ , and  $\boldsymbol{\epsilon}$ ) are Gaussian variables.

The temporal evolution of the state in space ( $\mathbf{x}$ ) and time ( $t$ ) through the dynamical model  $\mathbb{M}$  is denoted by eq. (1) up to a model error  $\mathbf{q}_t$ . In the context of this work, the state of the system denotes the velocity and pressure fields while the dynamical model is the NS equation given as,

$$\frac{\partial \mathbf{u}}{\partial t} + \mathbf{u} \cdot \nabla \mathbf{u} = -\frac{1}{\rho} \nabla p + \nu \Delta \mathbf{u}, \quad (4)$$

where  $\mathbf{u}$  is the velocity field,  $p$ , the pressure,  $\rho$ , the fluid density, and  $\nu$  stands for molecular viscosity. The model error is assumed to take the form of a centered Gaussian random variable with covariance  $\mathbf{Q}$ .

The second equation equates the state of the system at time  $t = 0$ , i.e.  $\boldsymbol{\chi}_0(\mathbf{x})$  to the *a priori* known background state  $\boldsymbol{\chi}_0^b(\mathbf{x})$  up to an error  $\boldsymbol{\eta}(\mathbf{x})$ . The background error is assumed to be of zero mean and associated to the background covariance matrix  $\mathbf{B}$  as,

$$\mathbf{B} = \mathbb{E}((\boldsymbol{\chi}_0^b - \boldsymbol{\chi}_0)(\boldsymbol{\chi}_0^b - \boldsymbol{\chi}_0)^T) = \mathbb{E}(\boldsymbol{\eta}\boldsymbol{\eta}^T). \quad (5)$$

The definition of this background covariance matrix is of significance in DA.  
 115 A method for defining this background covariance matrix using singular value decomposition (SVD) techniques is explored in §4.4.3.

The final equation relates the observations  $\mathbf{y}$  with the state variable  $\boldsymbol{\chi}$  through the observation operator  $\mathbb{H}$  which can be non-linear. This model is assumed to be accurate up to an observation error  $\boldsymbol{\epsilon}(t, \mathbf{x})$ . This error arises due  
 120 to sparseness of the observations, or due to scale dissimilarity between the observations and the state space or due to a noisy set of observations arising from experimental limitations. It covers equipment errors as well as errors arising from the observation operator. The error is assumed to be a zero mean Gaussian random field with the associated covariance tensor  $\mathbf{R}$ . All these Gaussian  
 125 assumptions on the different noises involved yields a joint probability distribution that can be expressed through its logarithm as a cost functional.

## 2.2. Cost Functional

The dynamical system is controlled by an initial condition and a forcing error term, which is a function of time and space. The cost function  $J(\boldsymbol{\eta}, \mathbf{q}_t)$  associated to these two unknown quantities can be expressed as:

$$J(\boldsymbol{\eta}, \mathbf{q}_t) = \frac{1}{2}(\boldsymbol{\mathcal{X}}_0 - \boldsymbol{\mathcal{X}}_0^b)^T \mathbf{B}^{-1}(\boldsymbol{\mathcal{X}}_0 - \boldsymbol{\mathcal{X}}_0^b) + \frac{1}{2} \int_{t_0}^{t_f} (\mathbb{H}(\boldsymbol{\mathcal{X}}_t) - \boldsymbol{\mathcal{Y}}_t)^T \mathbf{R}^{-1}(\mathbb{H}(\boldsymbol{\mathcal{X}}_t) - \boldsymbol{\mathcal{Y}}_t) + \frac{1}{2} \int_{t_0}^{t_f} \mathbf{q}_t^T \mathbf{Q}^{-1} \mathbf{q}_t, \quad (6)$$

where  $t_0$  and  $t_f$  are initial and final time of the assimilation window and the evolution of the state of the system  $\boldsymbol{\mathcal{X}}_t$  is given formally as,

$$\boldsymbol{\mathcal{X}}_t = \boldsymbol{\mathcal{X}}_0 + \int_{t_0}^t \mathbb{M}(\boldsymbol{\mathcal{X}}_s) ds + \int_{t_0}^t \mathbf{q}_s ds = \psi_t(\boldsymbol{\mathcal{X}}_0, \mathbf{q}_t), \quad (7)$$

where  $\psi_t(\boldsymbol{\mathcal{X}}_0, \mathbf{q}_t)$  is the flow map, which depends on the initial condition but also on the forcing along time.

130 The first term in the cost function accounts for the error between the initial condition  $\boldsymbol{\mathcal{X}}_0$  and the *a priori* known background condition  $\boldsymbol{\mathcal{X}}_0^b$  weighted by the inverse of the background error covariance matrix  $\mathbf{B}^{-1}$ . The second term is the error between the state trajectory  $\boldsymbol{\mathcal{X}}_t$  as obtained using the dynamical model ( $\mathbb{M}$ ) and the observations ( $\boldsymbol{\mathcal{Y}}$ ) using an appropriate observation operator ( $\mathbb{H}$ )  
135 and weighted by the inverse of the observation error covariance matrix  $\mathbf{R}^{-1}$ . The third term corresponds to the norm of the error forcing term weighted by the covariance matrix for the error model. Before entering into the details on why such a formulation is a bad idea for our application, we need to describe briefly in the following, the way the optimisation of such a functional can be  
140 performed in practice.

## 2.3. Adjoint method

To optimise the cost functional, a gradient descent methodology needs to be applied, which requires the explicit calculation of the gradient. Classical methods such as finite difference cannot be employed here - for DA studies of fluid

145 flows, the size of the state space could be of the order of  $10^{7-10}$  and successive integrations of the dynamics for each component of the initial condition are totally excluded. An elegant solution to do this at a reduced cost is the adjoint method, seminally proposed by Lions [27] and applied to the DA context by Le Dimet and Talagrand [26].

The adjoint model computes the gradient of the cost function in the direction  $\delta \mathbf{n} = (\delta \mathbf{q}_t, \delta \boldsymbol{\eta})$  with a single integration of the adjoint of the tangent linear dynamical model backwards in time. Consider an adjoint variable  $\boldsymbol{\lambda}$  belonging to the same state space and integrated over the time range of the assimilation, the inner product of this variable with tangent linear model of the non-linear dynamical model gives,

$$\int_{t_0}^{t_f} \left\langle \frac{\partial d\boldsymbol{\chi}_t}{\partial t}, \boldsymbol{\lambda}_t \right\rangle dt + \int_{t_0}^{t_f} \left\langle \partial_{\boldsymbol{\chi}} \mathbb{M} d\boldsymbol{\chi}_t, \boldsymbol{\lambda}_t \right\rangle dt = \int_{t_0}^{t_f} \left\langle \delta \mathbf{q}_t, \boldsymbol{\lambda}_t \right\rangle dt, \quad (8)$$

where,

$$\begin{aligned} \partial_t d\boldsymbol{\chi}(t, \mathbf{x}) + \partial_{\boldsymbol{\chi}} \mathbb{M}(\boldsymbol{\chi}(t, \mathbf{x})) d\boldsymbol{\chi}(t, \mathbf{x}) &= \delta \mathbf{q}_t(\mathbf{x}), \\ d\boldsymbol{\chi}(t_0, \mathbf{x}) &= \delta \boldsymbol{\eta}(\mathbf{x}), \end{aligned} \quad (9)$$

is the linear evolution model of the differential  $d\boldsymbol{\chi} = \partial_{\mathbf{q}} \mathbb{M} \delta \mathbf{q}_t + \partial_{\boldsymbol{\eta}} \mathbb{M} \delta \boldsymbol{\eta}$ , with  $\partial_{\boldsymbol{\chi}} \mathbb{M}$  denoting the tangent linear operator associated to the non-linear model operator  $\mathbb{M}$ , and  $\langle \cdot, \cdot \rangle$  stands for the  $\mathbb{L}^2$  inner product. The corresponding gradient of the tangent linear model along a direction  $\delta \mathbf{n}$  is,

$$\begin{aligned} \left\langle \frac{\partial J}{\partial \mathbf{n}}, \delta \mathbf{n} \right\rangle &= \left\langle \mathbf{B}^{-1}(\boldsymbol{\chi}_0 - \boldsymbol{\chi}_0^b), \delta \boldsymbol{\eta} \right\rangle - \int_{t_0}^{t_f} \left\langle (\partial_{\boldsymbol{\chi}} \mathbb{H})^* \mathbf{R}^{-1}(\mathbf{y}_t - \mathbb{H}(\boldsymbol{\chi}_t)), \frac{\partial \boldsymbol{\chi}}{\partial \mathbf{n}} \delta \mathbf{n} \right\rangle dt \\ &\quad + \int_{t_0}^{t_f} \left\langle \mathbf{Q}^{-1}(\partial_t \boldsymbol{\chi} + \mathbb{M}(\boldsymbol{\chi}_t)), \delta \mathbf{q}_t \right\rangle dt, \end{aligned} \quad (10)$$

where the adjoint operator of the for the linearised observation operator is introduced,

$$\left\langle (\partial_{\boldsymbol{\chi}} \mathbb{H}(\boldsymbol{\chi})) \mathbf{f}, \mathbf{g} \right\rangle = \left\langle \mathbf{f}, (\partial_{\boldsymbol{\chi}} \mathbb{H}(\boldsymbol{\chi}))^* \mathbf{g} \right\rangle. \quad (11)$$

Applying integration by parts to the right-hand side of (8) gives,

$$- \int_{t_0}^{t_f} \left\langle -\frac{\partial \boldsymbol{\lambda}_t}{\partial t} + (\partial_{\boldsymbol{\chi}} \mathbb{M})^* \boldsymbol{\lambda}_t, d\boldsymbol{\chi}_t \right\rangle dt = \langle \boldsymbol{\lambda}_{t_f}, d\boldsymbol{\chi}_{t_f} \rangle - \langle \boldsymbol{\lambda}_{t_0}, d\boldsymbol{\chi}_{t_0} \rangle + \int_{t_0}^{t_f} \langle \delta \mathbf{q}_t, \boldsymbol{\lambda}_t \rangle dt. \quad (12)$$

where  $(\partial_{\mathbf{x}}\mathbb{M})^*$  denotes the adjoint of the dynamics model tangent linear operator  $(\partial_{\mathbf{x}}\mathbb{M})$ . We impose the adjoint variable to be a solution of the following adjoint equation system:

$$\begin{cases} -\partial_t \boldsymbol{\lambda}_t + (\partial_{\mathbf{x}}\mathbb{M})^* \boldsymbol{\lambda}_t = (\partial_{\mathbf{x}}\mathbb{H})^* \mathbf{R}^{-1}(\mathbf{y} - \mathbb{H}(\mathbf{x}_t)), \\ \boldsymbol{\lambda}_{t_f} = 0. \end{cases} \quad (13)$$

We can now get the gradient of the cost function by inserting this relation in eq. (12) and equating  $d\mathbf{x}_{t_0} = \delta\boldsymbol{\eta}$  and  $d\mathbf{x} = (\partial\mathbf{x}/\partial\mathbf{n})\delta\mathbf{n}$  as,

$$\frac{\partial J}{\partial \boldsymbol{\eta}} = -\boldsymbol{\lambda}_{t_0} + \mathbf{B}^{-1}(\delta\mathbf{x}_0^b - \delta\mathbf{x}_0), \quad (14)$$

$$\frac{\partial J}{\partial \mathbf{q}} = \mathbf{Q}^{-1}(\partial_t \mathbf{x} + \mathbb{M}(\mathbf{x}_t)) - \boldsymbol{\lambda}. \quad (15)$$

150 To obtain the gradient of the cost function, a solution of the (backward) adjoint equation is necessary. However, through (15) we see that the knowledge of the whole adjoint variable must be computed and stored to get the gradient with respect to the error. Furthermore simulations of the forced dynamical system must be performed to evaluate the right-hand side of (13). The simulation of  
155 these two inter-dependant equations have to be performed until convergence.

Beyond the tricky character of this inter-dependance, in our case, at a more fundamental standpoint, the model error represents the error of the unresolved flow components whose action is nevertheless visible in the observations. They are associated to the fine scale flow structures and to turbulence. Due to the  
160 assumption introduced in this weakly constrained assimilation procedure, this turbulent component is represented by a Gaussian forcing variable, which is known to be a very restrictive assumption for turbulence modelling. A section of established turbulence models are based on a quasi-Gaussian hypothesis for turbulence closure. However, this is different from introducing directly a Gaussian forcing in data assimilation. The latter assumes that the contribution of  
165 the SGS terms is a Gaussian force which is a restrictive assumption. In addition, such a Gaussian forcing introduces additional energy in the system which is, in this case, not dissipated due to a lack of an additional dissipation term. In

the former case, Gaussian closure is used as a methodology to close the pdf of  
170 turbulence statistics. It is not achieved by adding a Gaussian variable directly  
in the equation. If we do apply a quasi-Gaussian hypothesis for turbulence  
closure and introduce such a model with the associated dissipation term, this  
would be along the same lines as this work albeit with a different model whose  
applicability will have to be analysed.

Given these restrictions, an alternative outlook is necessary to proceed fur-  
ther. Instead of a “blind” non-informative external Gaussian forcing, the error  
is now introduced directly in the model dynamics operator by replacing eq. (1)  
with:

$$\partial_t \mathcal{X} + \mathbb{M}(\mathcal{X}, \mathbf{q}_t) = 0. \quad (16)$$

In this system, we directly introduce the effect of the error on the dynamics  
through a function of the model error. We will see in section 3 how this can  
be precisely done for fluid dynamics through a stochastic framework that takes  
explicitly into account these errors. As a consequence, we revert back to a  
strong constraint assimilation problem. In its simplest expression, for a known  
characterisation of the error function, only the initial condition is an unknown  
variable, and we get back to a simplified functional of the form :

$$J(\boldsymbol{\eta}) = \frac{1}{2}(\boldsymbol{\mathcal{X}}_0 - \boldsymbol{\mathcal{X}}_0^b)^T \mathbf{B}^{-1}(\boldsymbol{\mathcal{X}}_0 - \boldsymbol{\mathcal{X}}_0^b) + \frac{1}{2} \int_{t_0}^{t_f} (\mathbb{H}(\boldsymbol{\mathcal{X}}_t) - \boldsymbol{\mathcal{Y}}_t)^T \mathbf{R}^{-1}(\mathbb{H}(\boldsymbol{\mathcal{X}}_t) - \boldsymbol{\mathcal{Y}}_t), \quad (17)$$

whose gradient with respect to the initial condition is given by:

$$\frac{\partial J}{\partial \boldsymbol{\eta}} = -\boldsymbol{\lambda}_{t_0} + \mathbf{B}^{-1}(\delta \boldsymbol{\mathcal{X}}_0^b - \delta \boldsymbol{\mathcal{X}}_0). \quad (18)$$

175 The gain in using the strong constraint procedure comes from two sources:  
firstly, the forcing in the weak procedure, that needs to be estimated at each  
time-step, is no longer explicit but integrated into the dynamical model, and  
secondly, the coupling of the inter-dependant equations (13) and (15) is elim-  
inated as the error is not a state variable in the strong-constraint procedure.  
180 This error can be optimised by introducing additional control variables in the  
assimilation but this is an optional control parameter.

#### 2.4. Additional control

When the error function is a priori not known, which is generally the case in practice, an additional control on the error function parameters  $\boldsymbol{\vartheta}_t$  can be introduced. Other parameters of the dynamical system related for instance to unknown inlet flow conditions can also be introduced through these additional control parameters. The dynamical model is now:

$$\partial_t \boldsymbol{\mathcal{X}}_t + \mathbb{M}(\boldsymbol{\mathcal{X}}_t, \boldsymbol{\vartheta}_t) = 0. \quad (19)$$

The new associated cost function, introduces a penalisation term on the error function,

$$J(\boldsymbol{\eta}, \boldsymbol{\vartheta}) = \frac{1}{2} \|\boldsymbol{\mathcal{X}}_0^b - \boldsymbol{\mathcal{X}}_0\|_{\mathbf{B}^{-1}}^2 + \frac{1}{2} \int_{t_0}^{t_f} \|\boldsymbol{\mathcal{Y}}_t - \mathbb{H}(\boldsymbol{\mathcal{X}}_t)\|_{\mathbf{R}^{-1}}^2 dt + \frac{1}{2} \int_{t_0}^{t_f} \|\boldsymbol{\vartheta}_t - \boldsymbol{\vartheta}_t^c\|_{\mathbf{B}_c^{-1}}^2 dt. \quad (20)$$

The cost function now has to minimise, alongside the background error  $\boldsymbol{\eta}$  and the observation error  $\boldsymbol{\epsilon}$ , the deviation of the control parameter from its *a priori* value ( $\boldsymbol{\vartheta}_t^c$ ) subject to a covariance  $\mathbf{B}_c$  as well,

The spatial support of the control parameter depends on the parameter considered. For an inlet flow control, the parameter is defined on the inlet plane of the computational domain while the coefficient of an error model can be defined over the entire spatial domain. The control parameter can also be stationary or temporally varying, thus requiring, in the latter case, an individual optimisation at each time-step - this can provide, for example, a gradually changing inflow condition capable of better capturing the optimal analysis trajectory.

By applying the adjoint formalism, taking into account the control parameters, the gradient can be evaluated as,

$$\frac{\partial J}{\partial \boldsymbol{\eta}} = -\boldsymbol{\lambda}_{t_0} + \mathbf{B}^{-1}(\boldsymbol{\mathcal{X}}_0^b - \boldsymbol{\mathcal{X}}_0), \quad (21)$$

$$\frac{\partial J}{\partial \boldsymbol{\vartheta}} = -\boldsymbol{\lambda}_{t_0} + \mathbf{B}_c^{-1}(\boldsymbol{\vartheta} - \boldsymbol{\vartheta}_c) + (\partial_{\boldsymbol{\vartheta}} \mathbb{M})^* \boldsymbol{\lambda}. \quad (22)$$

The adjoint methodology combined with the 4D-Var approach allows easy addition of control parameters provided the adjoint operator with respect to the



195 control parameter  $((\partial_{\theta}\mathbb{M})^*)$  can be constructed. The 4D-Var algorithm is depicted in figure 1.

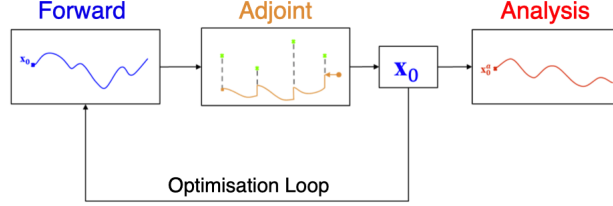


Figure 1: 4D-Var flow chart.

In order to perform data assimilation, the tangent linear and the adjoint version of the flow solver need to be constructed. The practical considerations behind this construction as well as with the optimisation procedure is presented in the next section.

### 2.5. Practical considerations

The construction of the adjoint model, for a dynamical model such as the Navier-Stokes equations, can be performed in two ways: the differentiate-then-discretise method involves the formulation of a mathematical adjoint which is then discretised on the numerical mesh while the discretise-then-differentiate method constructs the discrete (numerical) adjoint directly on the discretised non-linear model. In literature, the two methods are also referred to as continuous adjoint and discrete adjoint formulations respectively. Given a highly accurate numerical scheme, the discrete adjoint is capable of providing an accurate exact adjoint up to machine accuracy without any assumption (on the boundary conditions, for instance) unlike the continuous adjoint which is in general built from ideal boundary conditions. Thus, the discrete approach is preferred and the adjoint model is constructed using an automatic differentiation (AD) tool - TAPENADE [22]. The principles of AD and its application to VDA are briefly explained in the context of flow solvers in Chandramouli [5], Gronsks et al. [20]. Note that for reduced order formulation or ensemble assimilation techniques the

functional gradient can be directly computed [1, 11] or approximated through finite differences in the subspace spanned by the ensemble members [42, 43], respectively.

The adjoint trajectory in application requires the values of all intermediary variables obtained from the forward trajectory for each optimisation loop. Consider a non-linear dynamical model,

$$\mathbf{x}_0 \xrightarrow{I_1} \dots \xrightarrow{I_j} \mathbf{x}_j = I_j(\mathbf{x}_{j-1}) \xrightarrow{I_{j+1}} \dots \xrightarrow{I_f} \mathbf{x}_f, \quad (23)$$

the corresponding adjoint mode can be computed using,

$$\boldsymbol{\lambda}_0 \xleftarrow{I_1^*} \dots \xleftarrow{I_j^*} \boldsymbol{\lambda}_j = I_{j+1}^*(\mathbf{x}_{j-1}) \boldsymbol{\lambda}_{j+1} \xleftarrow{I_{j+1}^*} \dots \xleftarrow{I_f^*} \boldsymbol{\lambda}_f. \quad (24)$$

220 Thus to calculate  $\boldsymbol{\lambda}_j$ , the value of  $\mathbf{x}_{j-1}$  is required along with  $\boldsymbol{\lambda}_{j+1}$ . For a temporal model which is performed over sufficient number of time-steps the storing of these variables is problematic due to restrictive memory requirements. Such a method of storing all the intermediary values is termed as the ‘store-all’ strategy. A linear memory requirement increase is observed with increasing  
 225  $f$ . An alternative option of minimal energy storage is to recompute from the initial condition  $\mathbf{x}_0$  for every intermediary step  $j$ , the value of the variable  $\mathbf{x}_{j-1}$ . This strategy, termed as ‘recompute-all’ solves the memory overload issue, however, at the cost of high computational power. A brute-force strategy involving recompute-all has a quadratic relation between the computational cost  
 230 and number of intermediary steps.

For a Navier-Stokes solver, neither of these strategies are ideal. A combined strategy referred to as the ‘checkpointing’ strategy is used where the forward trajectory is check-pointed at specific intermediary points with the state variables stored in memory. All intermediary values between two checkpoints during the  
 235 adjoint trajectory can then be obtained by using either of the classical strategies depending on the restriction of memory or computational time.

Once the tangent linear model and the corresponding adjoint is constructed, the cost function and the gradient can be computed. The optimal solution is then obtained using an iterative optimisation method - the limited storage

240 gradient-based LBFGS optimisation method proposed by Nocedal [32] is implemented in this work.

## 2.6. Numerical solver

The 4D-Var algorithm developed in this work relies on the parallelised numerical solver, Incompact3d, developed by Laizet and Lamballais [25]. The solver resolves the full Navier-Stokes equation, i.e. direct numerical simulation (DNS), but its modularity allows for the easy addition of error model functions or turbulence models - this is important in the strong constraint assimilation problem considered here, where the error is introduced in the dynamics. The fortran based solver uses a cartesian mesh and sixth-order compact finite difference schemes for spatial discretisation. The incompressibility constraint is ensured by solving the Poisson equation in spectral space leading to an efficient yet inexpensive solution. The 4D-Var algorithm is enumerated in algorithm 1 and the forward and adjoint trajectories, respecting the modularity of Incompact3d, are depicted in figure 2.

---

### Algorithm 1 4D-Var algorithm with additional control variables

---

Initialisation:  $\mathbf{x}_0^{(1)} = \mathbf{x}_0^b$

**repeat**

    Forward evolution with the non-linear Navier-Stokes model

    Calculate cost functional  $J(\eta, \boldsymbol{\vartheta})$

    Backward evolution with the adjoint model - calculate  $\boldsymbol{\lambda}_{t_0}$

    Apply LBFGS algorithm

    Update initial condition:  $\mathbf{x}_0^{(k+1)} = \mathbf{x}_0^{(k)} + B\boldsymbol{\lambda}_{t_0}$

    Update control variable:  $\boldsymbol{\vartheta}^{(k+1)} = \boldsymbol{\vartheta}^{(k)} + B_c\boldsymbol{\lambda}_{t_0} - B_c(\partial_{\boldsymbol{\vartheta}}\mathbb{M})^*\boldsymbol{\lambda}$

**until**  $(\|\mathbf{x}_0^{(k+1)} - \mathbf{x}_0^{(k)}\|) < tol$

Forward integration of the non-linear dynamical model with  $\mathbf{x}_0^a = \mathbf{x}_0^{(k+1)}$  and  $\boldsymbol{\vartheta}^a = \boldsymbol{\vartheta}^{(k+1)}$  to get analysis trajectory  $\mathbf{x}_t^a$

---

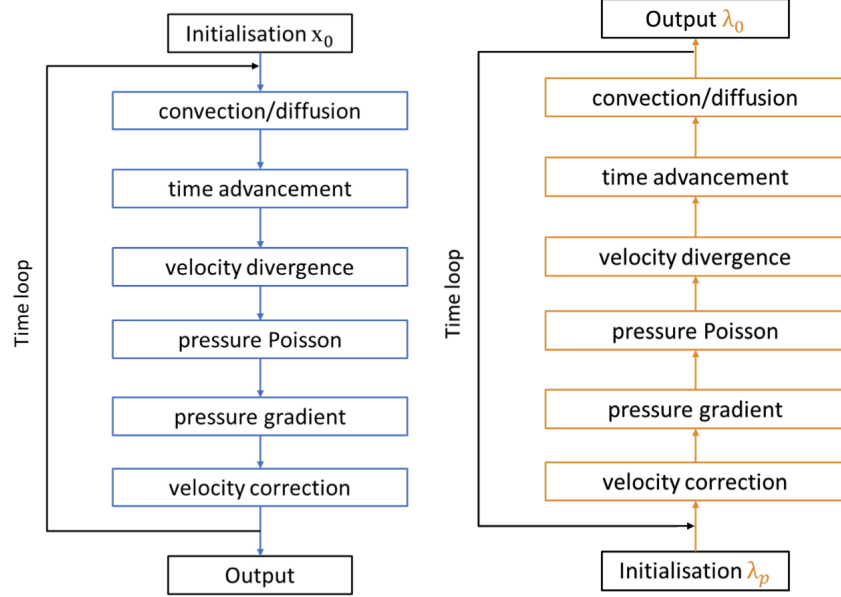


Figure 2: Flow chart for the forward (left) and backward (right) simulation with incompact3d.

### 255 3. Modelling under Location Uncertainty (LU)

The error modelling considered in the modified dynamics of our 4D-Var strategy is provided by the LU modelling framework of Mémin [29]. The LU model, in its grandest sense, presents a stochastic approach to turbulence modelling based on the decomposition of the velocity into a large-scale smooth component ( $\mathbf{u}$ ) and a small-scale highly oscillating random component ( $\sigma(\mathbf{X}_t, t)\dot{\mathbf{B}}$ ) representing the instantaneous error of the dynamical system:

$$\frac{d\mathbf{X}_t}{dt} = \mathbf{u}(\mathbf{X}_t, t) + \underbrace{\sigma(\mathbf{X}_t, t)\dot{\mathbf{B}}}_{\mathbf{q}_t}. \quad (25)$$

This decomposition of the Lagrangian velocity in terms of a smooth component and a time uncorrelated random error component, leads to a stochastic representation (in the Ito setting) of the rate of change of a scalar quantity transported by the random flow. This is essentially a stochastic representation of the Reynolds transport theorem (RTT) (see Mémin [29], Resseguier et al. [36] for a complete derivation). This stochastic RTT allows us to derive a

stochastic mass conservation equation and, from the Newton second principle (in a distributional sense), a stochastic Navier-Stokes system of equations for an incompressible fluid [29]

$$\nabla \cdot \mathbf{u} = 0; \quad \nabla \cdot (\nabla \cdot \mathbf{a}) = 0; \quad \nabla \cdot (\mathbf{q}_t) = 0; \quad (26)$$

$$d_t \mathbf{u} + ((\mathbf{u}^* dt + \mathbf{q}_t) \cdot \nabla) \mathbf{u} - \frac{1}{2} \nabla \cdot ((\mathbf{a} \nabla) \mathbf{u}) dt = -\frac{1}{\rho} \nabla p + \nu \Delta (\mathbf{u} dt + \mathbf{q}_t), \quad (27)$$

where  $d_t \mathbf{u}$  is the time increment at a given point in space of the velocity, and  $\mathbf{u}^*$  is the modified advection defined as:

$$\mathbf{u}^* = \mathbf{u} - \frac{1}{2} \nabla \cdot \mathbf{a}, \quad (28)$$

where the variance tensor  $\mathbf{a}(\mathbf{x}, t)$  is a  $3 \times 3$  symmetric positive definite matrix of finite variation (i.e. they are similar to deterministic functions) directly related to the variance of the error term (i.e. the unresolved velocity component):  $\mathbf{a}(\mathbf{x}, t) dt = \mathbb{E}(\mathbf{q}_t(\mathbf{x}) \mathbf{q}_t(\mathbf{x})^T)$ . This variance tensor has the dimensions of kinematic viscosity  $[m^2 s^{-1}]$  and plays a role similar to the eddy viscosity of classical LES models.

Assuming in addition that the resolved velocity component,  $\mathbf{u}$ , is also of finite variation allows us to safely separate this system in terms of deterministic momentum equations and a stochastic balance:

$$\partial_t \mathbf{u} + \mathbf{u}^* \cdot \nabla \mathbf{u} - \frac{1}{2} \sum_{ij} \partial_{x_i} (a_{ij} \partial_{x_j} \mathbf{u}) = \frac{1}{\rho} \nabla p + \nu \Delta \mathbf{u}, \quad (29)$$

$$\frac{1}{\rho} \nabla p' = -\mathbf{q}_t \cdot \nabla \mathbf{u} + \nu \Delta (\mathbf{q}_t). \quad (30)$$

This deterministic system is fully determined by the knowledge of the variance tensor  $\mathbf{a}$ . The stochastic balance equation (30) enables, with an expression of the diffusion tensor, to get an expression of the turbulent pressure  $p'$ . However, its knowledge is not required in the momentum equation, and this balance equation will not be used further.

Let us note that relaxing the bounded variation assumption for the resolved component requires to use the full stochastic expression of the momentum equation as in [6, 9].

The set of deterministic conservations equations (eq. (26) and (29)) can be closed by modelling the variance tensor  $\mathbf{a}$ . Various closure models are presented in Chandramouli et al. [8], of which the stochastic spatial variance (StSp) model was best suited for cylinder wake flow - hence, this is chosen here for modelling  $\mathbf{a}$ . In this model, the variance tensor is calculated as a local spatial variance based on the resolved velocity field:

$$\mathbf{a}(\mathbf{x}, t) = \frac{1}{|\Gamma| - 1} \sum_{x_i \in \Gamma(\mathbf{x})} (\mathbf{u}(x_i, t) - \mathbf{u}_m(x, t))(\mathbf{u}(x_i, t) - \mathbf{u}_m(x, t))^T C_{sp}, \quad (31)$$

where  $\mathbf{u}_m(x, t)$  stands for the empirical mean on the arbitrarily selected local spatial neighbourhood defined by  $\Gamma$ . Through dimensional arguments, the coefficient  $C_{sp}$  is defined as [23]:

$$C_{sp} = \left( \frac{\ell_{res}}{\ell_{kol}} \right)^{\frac{5}{3}} \Delta t, \quad (32)$$

where  $\ell_{res}$  is the resolved length scale,  $\ell_{kol}$  is the Kolmogorov length scale and  $\Delta t$  is the simulation time step. In §5, this stationary coefficient is assumed to be spatially varying but unknown and is estimated using the 4D-Var algorithm. **This coefficient corresponds to the control parameter associated to the model error.** An added advantage of using this model in 4D-Var is the simplicity of implementation as compared to certain models such as the dynamic Smagorinsky sub-grid model which requires filtering and thresholding operations. In order to perform the adjoint of such a model, the corresponding adjoint code formulation needs to be developed accounting for these addition operations which is not straightforward [24].

The full mathematical derivation of the model can be found in Mémin [29], its successful application to geophysical flows in Resseguier et al. [35, 36, 37] and to industrial/engineering flows in Chandramouli et al. [8], Kadri Harouna and Mémin [23].

#### 4. 4D assimilation of a wake flow

285 The various ingredients required for performing 4D-Var are now presented briefly. This is followed by assimilation results assessing the performance of the algorithm with respect to different parameters: quality of background condition, quality of observations, and background covariance matrices. The assimilation experiments will be conducted in two different situations.

- 290 • An idealised case for which a 3D volume of velocity measurements will be assumed to be available.
- A realistic configuration in which only two orthogonal planes of 3D velocity measurements (2D-3C PIV-like) will be accessible.

The first case will allow us to have an ideal “best” case for the assimilation, 295 to which we will compare the second that corresponds to an experimentally realistic situation.

##### 4.1. Flow Configuration:

The experimentation will be conducted on the wake flow over a circular cylinder with reference data. This flow configuration is well-studied for data- 300 assimilation studies and reduced order modelling analyses [17, 41, 20]. To build this reference data, the flow is simulated over a large domain to measure and store velocity fields at regular intervals corresponding to observations. This large domain includes the obstacle whereas the assimilation will be performed on a smaller domain in the wake **without any modelling of the obstacle**.

305 To include the obstacle geometry in 4D-Var would require the numerical adjoint of the method, such as IBM, used to account for the geometry. However, given no information of the obstacle, to reconstruct the flow field is a unique challenge in its own respect and is what is addressed in this work. All simulations are performed using the parallelised flow solver, Incompact3d.

310 For obtaining the reference data, the flow over the cylinder is simulated for a Re of 3900 on a domain measuring  $20D \times 20D \times \pi D$ . Due to the restrictive

cost of DNS, an LES is performed using the LU model (StSp model of Chandramouli et al. [8]) with the domain discretised into  $241 \times 241 \times 48$  points with stretching implemented in the lateral direction. In Kolmogorov units ( $\eta_k$ ),  
315 with  $\eta_k$  calculated from dissipation rate and viscosity, the mesh resolution is  $41\eta_k \times 7\eta_k - 60\eta_k \times 32\eta_k$ . The cylinder is placed in the centre of the lateral domain at 10D and at 5D from the streamwise domain inlet. In this simulation for the reference, the Immersed Boundary Method (IBM) developed by Gautier et al. [18] is used to emulate a body forcing to incorporate the solid boundaries  
320 of the cylinder. Inflow/outflow boundary conditions are implemented along the streamwise (x) direction with free-slip and periodic boundary conditions along the lateral (y) and spanwise (z) directions respectively. The turbulence is initiated in the flow via a white noise in the initial condition. Time advancement is performed using the third order Adams-Bashforth (AB3) scheme. For the LES  
325 model, a spatial neighbourhood spanning  $7 \times 7 \times 7$  points is used for the averaging and variance calculations. For this data collection step, the coefficient for the model is defined based on the Kolmogorov length and time scales (see eq. (32)). This simulation has been shown to provide better results than classical LES schemes [8, 23].

330 In the assimilation step, a smaller domain in the near wake of the cylinder starting at 3D length behind the cylinder was chosen. The goal being to assess the method in a configuration for which the obstacle geometry is not modelled nor precisely known. This assimilation sub-domain measures  $6D \times 6D \times \pi D$  and is discretised into  $165 \times 165 \times 48$  (see figure 3). The mesh for assimilation is not  
335 stretched and the data of the reference simulation are thus properly interpolated to fit the non stretched assimilation domain. The resolution of the assimilation mesh is  $18\eta_k \times 18\eta_k \times 32\eta_k$ . This resolution is finer along the streamwise direction and same along the spanwise direction in comparison with the reference. Along the lateral direction, the uniform size of  $18\eta_k$  is in the middle of the varying resolution of the stretched mesh for the reference ( $12\eta_k \times 38\eta_k$ ) in the assimilation  
340 domain. For the forward trajectory of the assimilation, inflow/outflow, free-slip, and periodic boundary conditions are implemented in the streamwise, lateral,



and spanwise directions respectively. The numerical adjoint of these boundary conditions are developed with the AD tool for the backward trajectory. The  
 345 choice of free-slip boundary condition is applicable for the assimilation provided that the vortex street does not cross the lateral boundary. The AB3 scheme and its adjoint are used for the forward and backward trajectories respectively.

The non-stretched mesh together with the imprecise boundary conditions yields inherent discrepancy between the reference model and the assimilation  
 350 error model. The assimilation is carried out on this domain using the StSp model (eq. (31) for the variance tensor  $\mathbf{a}$ ) for which a constant initial coefficient is fixed based on the scaling of eq. (32). It is important to note that only the three-component velocity fields will be observed in the assimilation window. All the other quantities required for the restart procedure of Incompact3d at the  
 355 beginning of the assimilation window (pressure field, convection and diffusion terms of previous time-steps, etc) are assumed to be completely unknown and hence set to zero. This contributes as well to an additional strong discrepancy between the reference and assimilation models. The spatial parameters for the reference and assimilation domain are tabulated in table 1.

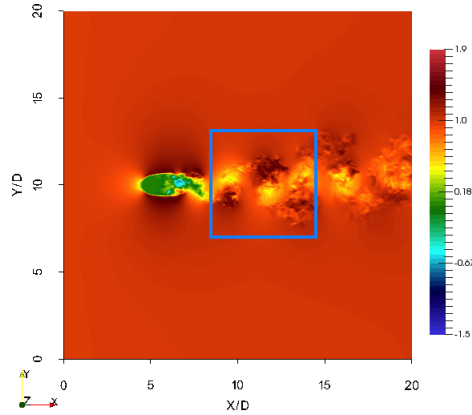


Figure 3: Streamwise velocity snapshot in the reference domain with the cylinder at a  $(x,y)$  of  $(5D, 10D)$ . The sub-domain in blue corresponds to the assimilation domain; Observation data are extracted in this domain.

Table 1: Configuration parameters for the reference and assimilation runs.

	Re	$n_x \times n_y \times n_z$	$l_x/D \times l_y/D \times l_z/D$	$U\Delta t/D$	Duration
Reference data constitution	3900	$241 \times 241^s \times 48$	$20 \times 20 \times 3.14$	0.003	$30100\Delta t$
Data extraction	3900	$165^i \times 165^i \times 48$	$6 \times 6 \times 3.14$	0.003	$100\Delta t$
4D-Var	3900	$165 \times 165 \times 48$	$6 \times 6 \times 3.14$	0.003	$100\Delta t$

s - Stretched; i - Interpolated

#### 4.2. Observation data

The data-extraction step provides 3D observation data over the domain of interest for the time-period of the assimilation, i.e. the reference ( $Obs_{true}$ ). It is important to note that in the smaller assimilation domain, the boundary conditions do not correspond perfectly to the boundary conditions imposed in the solver due to the smaller size of the assimilation domain. These boundary condition effects are taken into account through the inverse of the observation covariance matrix  $\mathbf{R}_{3D}^{-1}$  which reduces confidence on the observations closer to the boundaries. The expression for  $\mathbf{R}_{3D}^{-1}$  is provided in the appendix and pictured in figure 5. This 3D data-set with the associated covariance matrix can be used in the assimilation algorithm to assess the capabilities of the optimisation procedure. This corresponds to the ideal case setup.

As for the second experimentally realistic case, observations emulating the sparsity of cross-plane 2D3C stereoscopic PIV measurements are obtained from the reference observations by extracting velocity fields on two perpendicular planes situated at the inlet (XZ) and in the middle of the spanwise domain (XY). The direct use of such sparse data in VDA, while feasible, is not advisable. With limited spatial observations, the information needs to be transferred efficiently to the entire physical domain. This can be achieved by using a well-defined observation covariance matrix but the expression of such a covariance matrix can be difficult to obtain. Another option, as implemented by Meldi and Poux [28], is to use the pressure-velocity relation to propagate the information globally via the poisson solver. However, such a propagation accepts a significantly wide

range of acceptable solutions which may not be close to the true state of the system. In this work, we opt rather for the fast snapshot optimisation (SO) algorithm proposed by Chandramouli et al. [7] to reconstruct the unknown 3D volume given the information on the two cross-planes ( $Obs_{rec}$ ). The SO method exploits the homogeneity along the spanwise direction for cylinder wake in order to identify from a long sequence of 2D observations the optimal match using a gradient descent methodology. Such an algorithm manages to reconstruct major turbulent structures in the flow with a low computational cost. The advantage of such a reconstruction lies in the additional information that is provided to the assimilation algorithm - namely the presence of temporal and spanwise spatial homogeneity. An alternative weighted gaussian interpolation methodology is also used to reconstruct the 3D domain ( $Obs_{inter}$ ) given 2D planar fields to facilitate a comparison with the SO reconstructed observations (see appendix for a description of the interpolation method used). For both of these observations, the confidence on the data is reflected on  $\mathbf{R}_{PIV}^{-1}$  with reduced values at all points except on the two cross-planes of true data. A 2D ( $XY$ ) view of the three types of observations at  $z = 1.31D$  are shown in figure 4. The inverse of the observation covariance matrices for the different types of observations are shown in figure 5 - to reiterate,  $\mathbf{R}_{3D}^{-1}$ , corresponding to the ‘ideal’ case, retains maximum confidence on the data within the assimilation domain with reduced confidence on the boundaries while  $\mathbf{R}_{PIV}^{-1}$ , corresponding to the ‘realistic’ case, reflects high confidence only for data on the two planes on which the three components of velocity are extracted (the precise expression for  $\mathbf{R}_{3D}^{-1}$  and  $\mathbf{R}_{PIV}^{-1}$  are provided in the appendix). The offset for visualisation from the mid-plane at  $z = 1.57D$  is needed to emphasise the difference between the three kinds of observations which are identical in the spanwise mid-plane. Henceforth all velocity field visualisation are done on the  $XY$  plane at  $z = 1.31D$  unless mentioned otherwise.

Discontinuities can be seen in the velocity fields with the interpolation algorithm that are non-physical. This artefact is strengthened in the outlet velocity fields shown in figure 6 for the three observations. The interpolation downstream

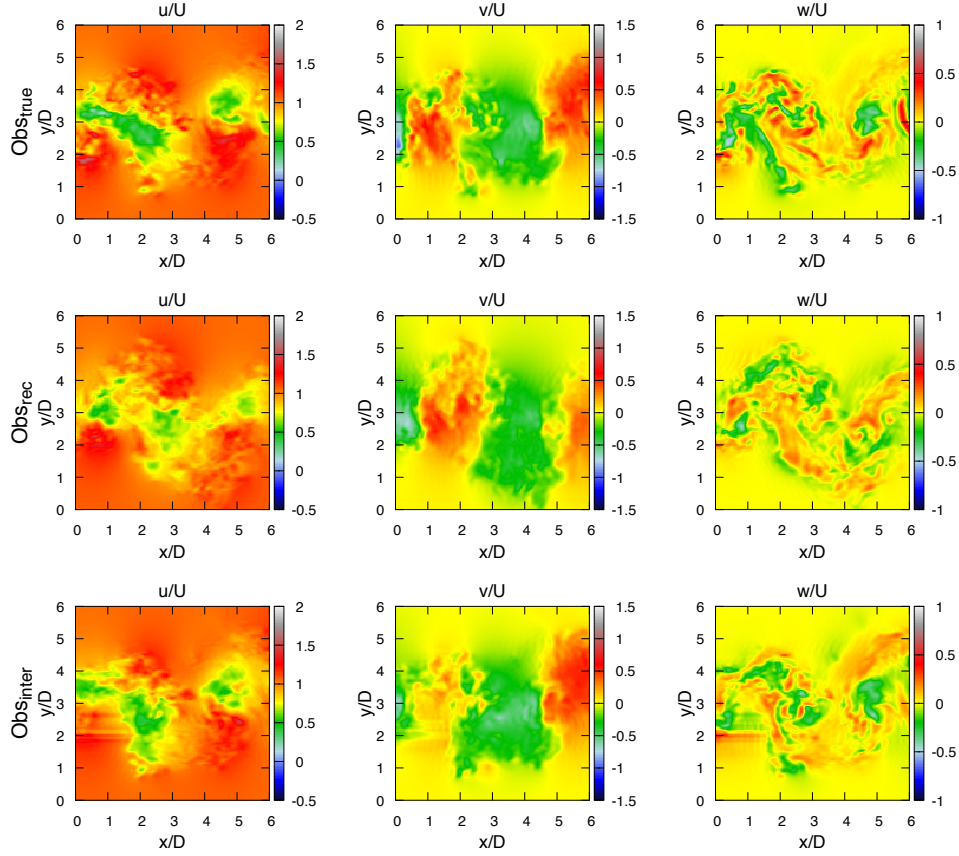


Figure 4: Observation velocity snapshots at the beginning of the assimilation window ( $t'_1$ ) in the plane  $z = 1.31D$ . From left to right: streamwise, lateral, and spanwise fields. From top to bottom:  $Obs_{true}$ ,  $Obs_{rec}$ , and  $Obs_{inter}$

from the inlet simply mirrors the observation plane leading to unphysical obser-  
415 vations. The SO algorithm is able to roughly reconstruct turbulent structures  
that are representative of the flow. The effect of the quality of observations on  
the assimilation algorithm is analysed in §4.4.2.

#### 4.3. Background data

An accurate background condition provides a good starting point for the as-  
420 simulation algorithm leading to faster convergence while an inaccurate condition,  
which is too far from the optima, can restrict and destabilise the algorithm. For

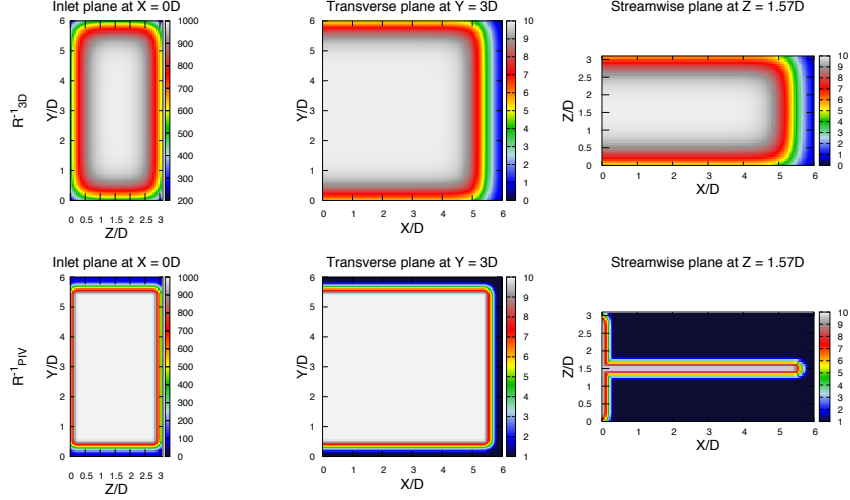


Figure 5: Confidence on the observed velocity fields denoted by  $\mathbf{R}^{-1}$ . From left to right: inlet plane at  $x = 0D$ , transverse plane at  $y = 3D$ , and streamwise plane at  $z = 1.57D$ . From top to bottom:  $\mathbf{R}_{3D}^{-1}$ , and  $\mathbf{R}_{PIV}^{-1}$

initial tests with volumetric observations, the background condition is obtained by biasing the true velocity maps by a sinusoidal wave. This ‘incorrect’ or biased background ( $Bg_{bias}$ ) condition provides an opportunity to test algorithm stability and accuracy in the validation study to follow.

Experimentally, it is hardly feasible, and only at high computational cost, to have 3D observations from which a background condition can be obtained. Such a 3D initial background, which is required for 4D-Var, can be obtained through 3D tomographic PIV techniques [12] or through numerical simulation, where the flow is simulated from a precise, temporally highly resolved, inlet condition until the entire domain is filled. Both techniques are computationally very costly. An alternate solution, drawing inspiration from the observation reconstruction, is to use the SO method to reconstruct the volume with 2D planar data. Such a background condition ( $Bg_{rec}$ ) can be obtained in a very fast way and constitute a good representation of the flow condition. The three components of the two background conditions are shown in figure 7. The dependency of the 4D-Var algorithm on the quality of the background condition is analysed in §4.4.1.

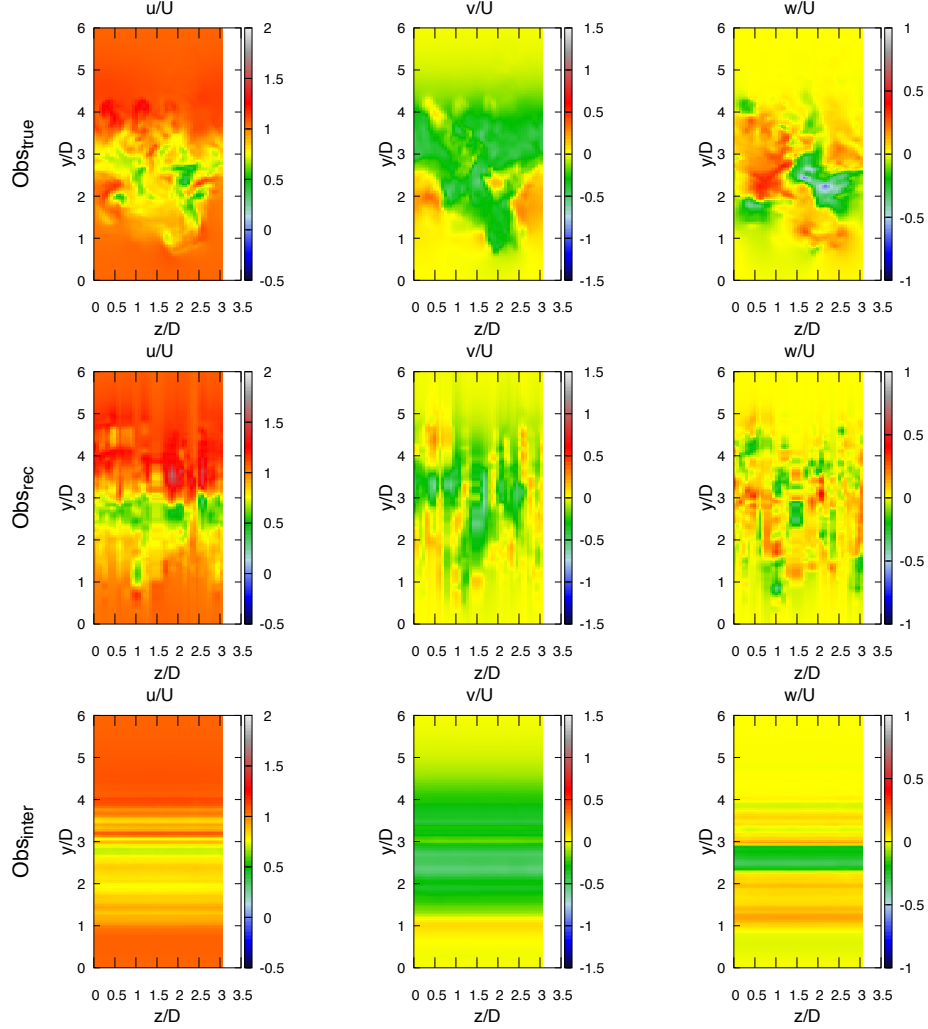


Figure 6: Observation velocity snapshots at the beginning of the assimilation window ( $t'_1$ ) in the plane  $x = 6D$  (at the outlet). From left to right: streamwise, lateral, and spanwise fields. From top to bottom:  $Obs_{true}$ ,  $Obs_{rec}$ ,  $Obs_{inter}$ .

The definition of the inverse of the background covariance matrix  $B^{-1}$  and the associated implication on the 4D-Var algorithm is dealt with in section 4.4.3.

440 For results presented in §4.4.1 and §4.4.2, this matrix is set to be identity - i.e. each point in space is independent of other points in space and a change at one point has no direct effect on the neighbouring points. We present now the

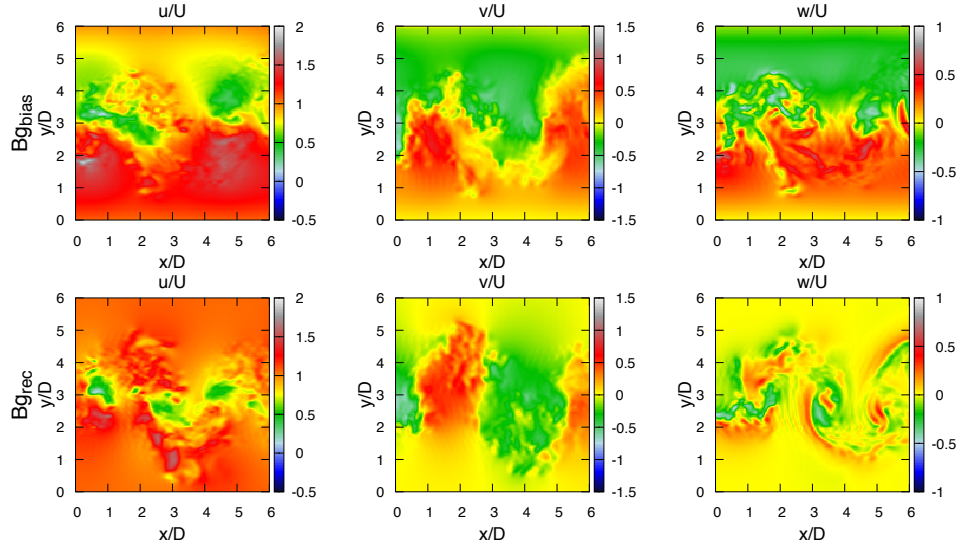


Figure 7: Background velocity snapshots at the beginning of the assimilation window ( $t'_1$ ) in the plane  $z = 1.31D$ . From left to right: streamwise, lateral, and spanwise fields. From top to bottom:  $Bg_{bias}$ , and  $Bg_{rec}$

algorithm results via an analysis of three essential parameters for 4D-Var: the background condition, the observation data-set, and the background covariance matrix.

#### 4.4. 4D-Var results

##### 4.4.1. Analysis 1 - Background condition

The first parameter analysed is the background condition and the effect of its quality on the assimilation results. This section aims to answer the following questions:

- How important is the quality of the background condition?
- What is its effect in terms of accuracy and cost for 4D-Var?
- Is algorithm stability correlated with the background condition?

We perform two simulations with identical parameters using  $Obs_{true}$  for both while varying the background condition. For case (a), we use the biased

Table 2: Parameters for the different assimilation cases.

Case	Observations	Background	Background covariance	Coefficient optimisation
(a)	$Obs_{true}$	$Bg_{bias}$	Identity	No
(b)	$Obs_{true}$	$Bg_{rec}$	Identity	No
(c)	$Obs_{inter}$	$Bg_{rec}$	Identity	No
(d)	$Obs_{rec}$	$Bg_{rec}$	Identity	No
(e)	$Obs_{true}$	$Bg_{rec}$	Fully-defined	No
(f)	$Obs_{rec}$	$Bg_{rec}$	Fully-defined	Yes

background while for case (b) we use the reconstructed background using the SO methodology. The parameters of all cases studied in this article are presented concisely in table 2. Neither background condition is a perfect representation of the initial flow state but it can be argued that the deviations introduced by the bias are non-physical while the reconstructed rough background only introduces a phase-change - i.e. a representation of the flow at a different time with minor discontinuities in the spanwise directions. Case (a) is a test for the algorithm in terms of stability and capability to recover the reference state given an incorrect initial condition. Case (b) aims to explore the importance of the quality of the background condition and its effect on the accuracy and cost of the 4D-Var algorithm.

The optimisation characteristics, namely the cost function ( $J(\mathcal{X}_0)$ ) and its gradient ( $||\nabla J(\mathcal{X}_0)||$ ), are plotted as a function of the inner loop iterations in figure 8. As can be expected, a direct correlation is observed between the quality of the background and the iterations required to converge to a solution - case (b) requires only half of the iterations of case (a) to converge. The final cost of the analysis trajectory (analysis refers to the final estimate of the velocity field obtained from the assimilation) are similar for both cases. For case (a), the mismatch between the observations and the background manifests as peaks in the cost functional compared to the smooth decline for case (b). These peaks occur



due to very strong gradients, which alter the gradient descent procedure. These gradients can be associated to the unphysical background condition provided to the procedure which does not respect the dynamical model.

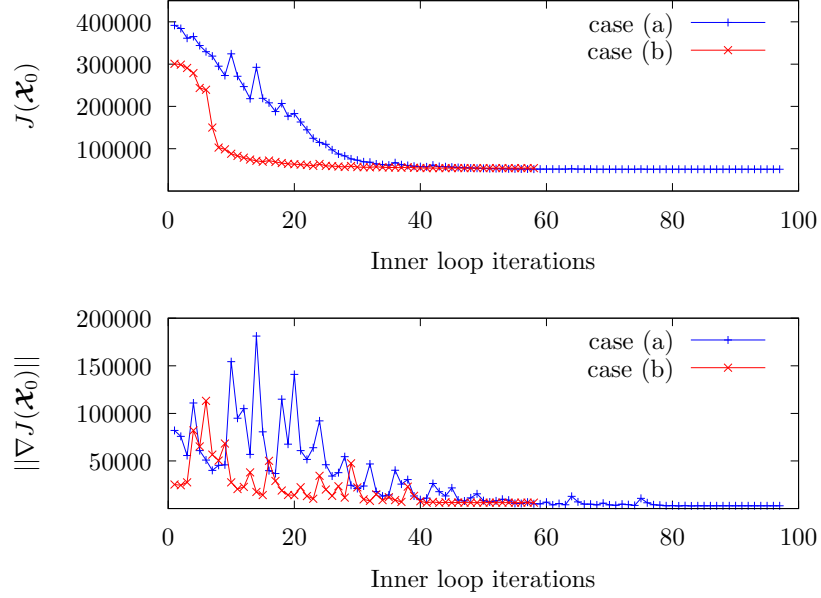


Figure 8: Evolution of the cost function  $J(\mathbf{x}_0)$  and its gradient  $||\nabla J(\mathbf{x}_0)||$  for the assimilation as a function of inner loop iterations for cases (a) and (b).

The analysis velocity field maps for the two cases ( $An_{case(a)}$ , and  $An_{case(b)}$ ),  
 480 are shown in figure 9 along with the corresponding background maps and the  
 reference state. There is a marked improvement from the background to the  
 analysis contour maps especially for case (b) where we observe a near-perfect  
 match with the reference. The analysis maps suggests that an incorrect but  
 physically meaningful representation of the flow enables to improve the accuracy  
 485 of the assimilation results. The algorithm, while remaining globally stable (i.e.  
 the sharp peaks due to high gradients do not alter the global convergence) for the  
 biased background, does not manage to identify an accurate initial condition.  
 However, at the end of the assimilation window, we obtain velocity maps for both  
 cases that match well with the reference (see figure 10). This result highlights

490 the capabilities of the 4D-Var algorithm to produce meaningful results with incorrect data-sets.

#### 4.4.2. Analysis 2 - Observation data-set

3D, accurate measurements of variables of interest in the assimilation domain are difficult to obtain with existing methodologies. While simulations can provide these quantities, their accuracy will be dependant on the boundary condition errors and other numerical errors. 3D flow measurement techniques, such as tomo-PIV, are computationally expensive techniques and are still restricted in their application to small domain or sparse data. However, to obtain 2D3C data on cross-planes, quick and efficient established stereoscopic PIV techniques are available. Computationally efficient assimilation algorithm must thus be defined from such sparse observations or at least from a low cost volumetric reconstruction from these 2D data. The ability of the 4D-Var algorithm to work with such data is analysed here wherein we try to answer the following:

- Can simple mathematical techniques such as interpolation methods provide acceptable volumetric observations?
- Are SO reconstructed observations better suited for 4D-Var?
- Is there a correlation between stability of the algorithm and quality of the observations?

Two additional assimilation studies are performed: case (c) with interpolated observations ( $Obs_{inter}$ ) and case (d) with reconstructed observations ( $Obs_{rec}$ ). Identical flow and optimisation parameters are provided to both cases with the  $Bg_{rec}$  background condition. In both cases, the 3D reference has not been provided. Both the observations and the background are only an expectation of the 3D flow field as is the case with assimilation of experimental observations.

515 The optimisation characteristics in figure 11 show similar convergence for both cases with a few additional iterations for case (d) and a final cost that is marginally higher for case (c) as compared to case (d). For case (c), we note

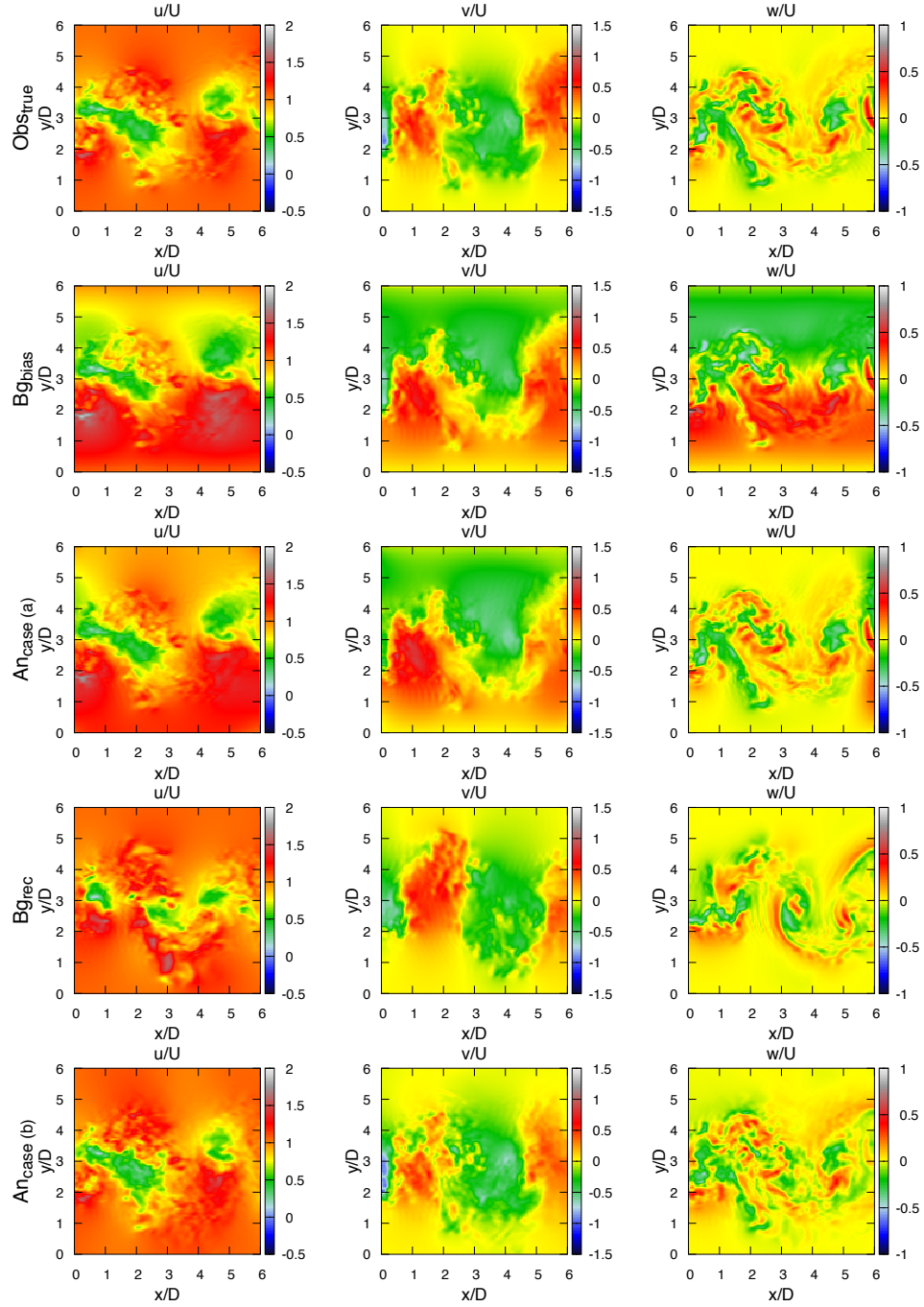


Figure 9: Velocity snapshots at the beginning of the assimilation window ( $t'_1$ ) in the plane  $z = 1.31D$ . From left to right: streamwise, lateral, and spanwise fields. From top to bottom: *Obstrue*, *Bgbias*, *An<sub>case</sub> (a)*, *Bgrec* and *An<sub>case</sub> (b)*

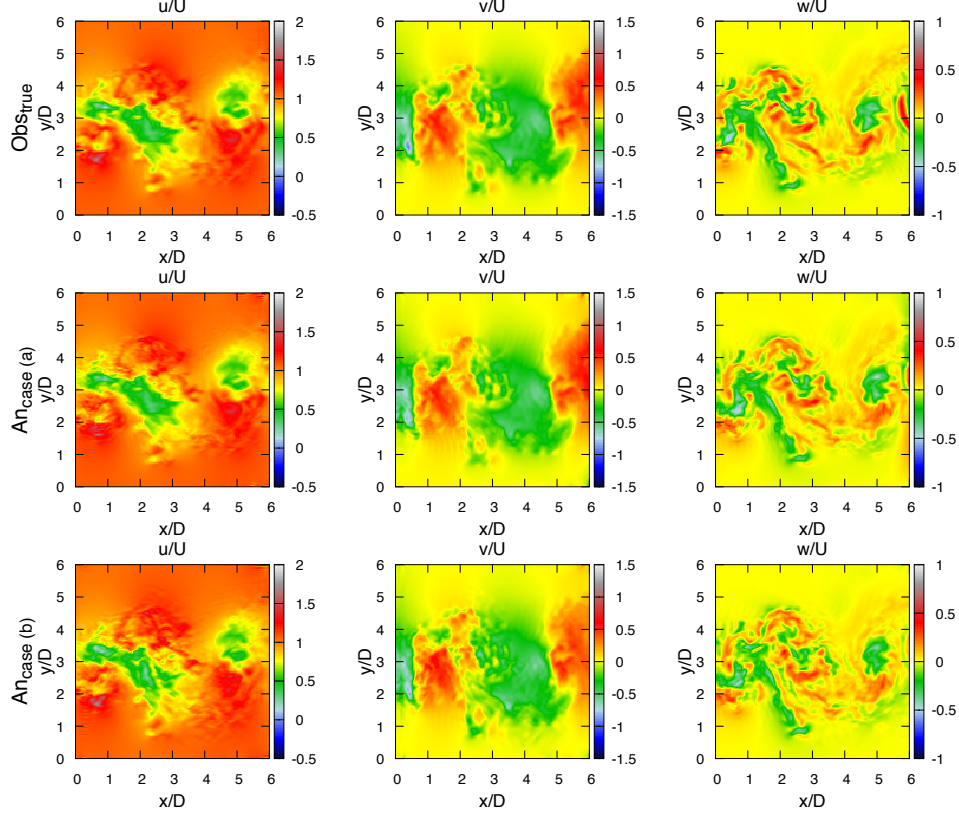


Figure 10: Velocity snapshots at the end of the assimilation window ( $t'_1$ ) in the plane  $z = 1.31D$ . From left to right: streamwise, lateral, and spanwise fields. From top to bottom:  $Obs_{true}$ ,  $An_{case} (a)$ , and  $An_{case} (b)$

that a high gradient peak perturbs the gradient descent which is likely due to unphysical observations associated to the interpolation procedure. These characteristics suggests that simple mathematical techniques such as interpolation methods provide satisfactory observations for assimilation. We also observe that the analysis velocity maps obtained with both cases (see figure 12) are quite similar - the analysis is a compromise between the background and the observations, constrained by the governing equations. **The forward evolution in time of the full nonlinear dynamics from the analysis initial condition, however, introduces instabilities for case (c) leading to a**

numerical explosion unlike case (d) which remains stable. These instability issues, due again probably to unphysical forcing, prevent thus the practical use of interpolated data. The analysis velocity maps for case (d) at the end of the assimilation window is shown in figure 13.

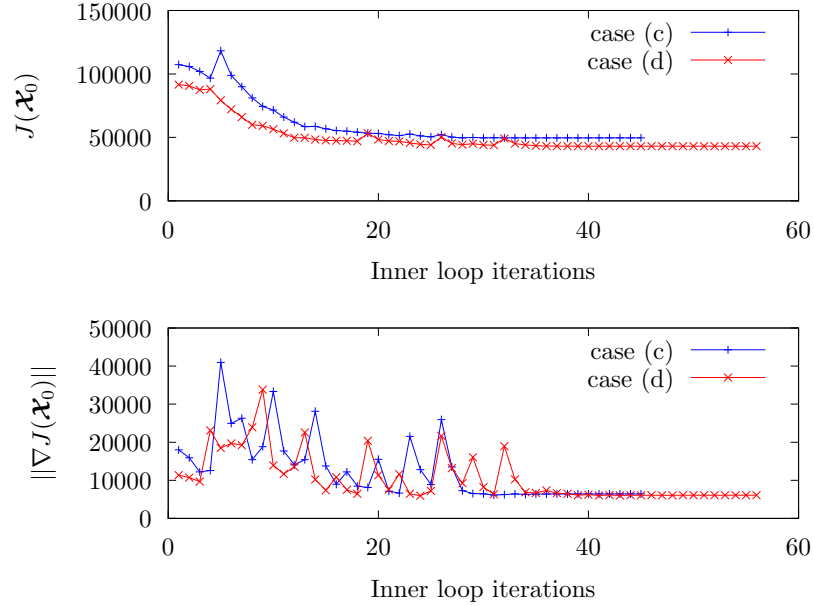


Figure 11: Evolution of the cost function  $J(\mathbf{x}_0)$  and its gradient  $\|\nabla J(\mathbf{x}_0)\|$  for the assimilation as a function of inner loop iterations for cases (c) and (d).

The root-mean-square-error (RMSE) evolution along time between the background, observation, and analysis trajectories with the true observations are plotted in figure 14 for the three velocity components for case (d). The RMSE for the analysis (in red) has the lowest error with significant improvement over the background. The analysis is the best estimate for the spanwise component as the observations, which are constructed using the SO algorithm, do not ensure a divergence free flow. The 4D-Var analysis is subject to the divergence free criterion by the solver and thus predicts an improved trajectory for the spanwise velocity component.

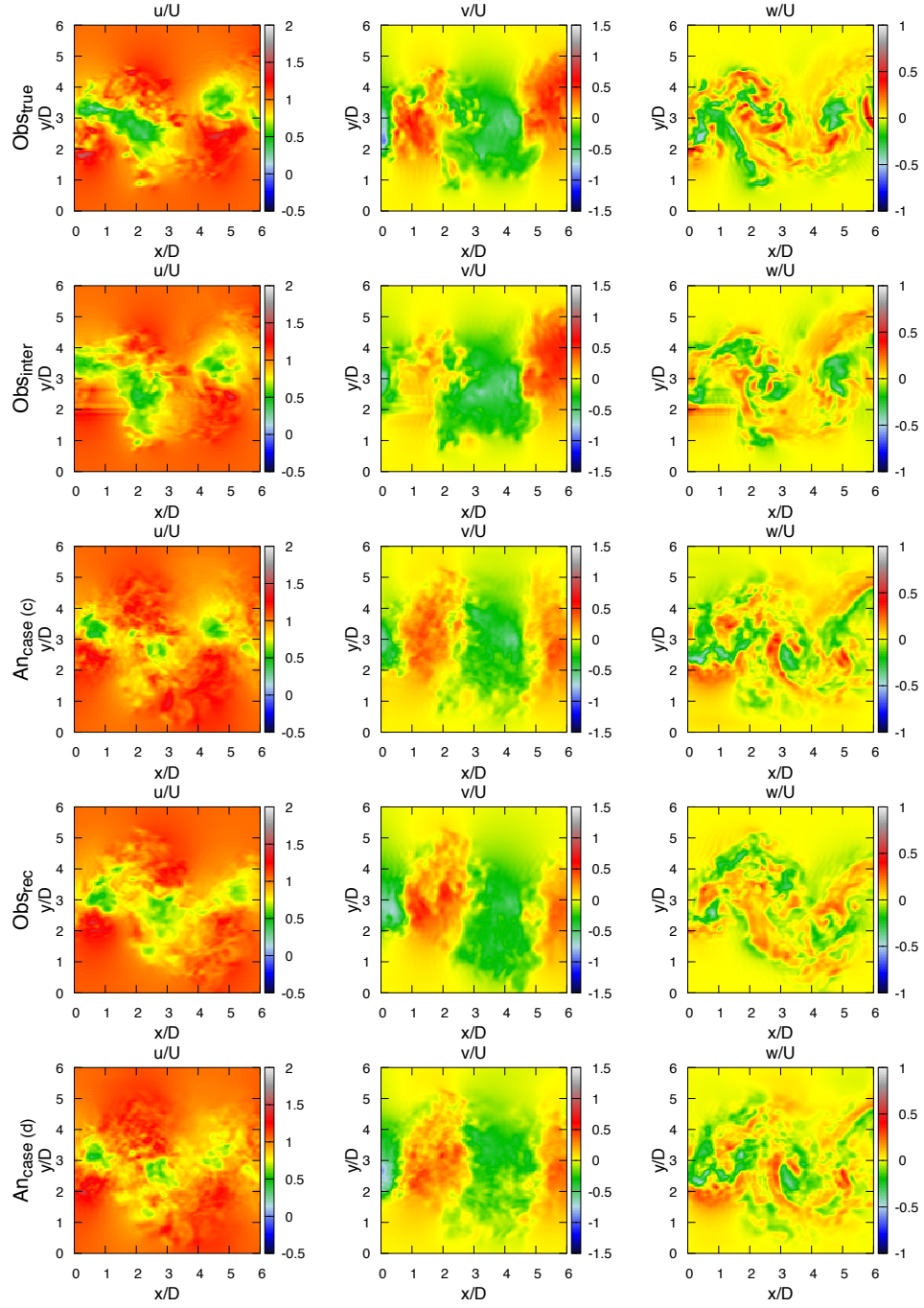


Figure 12: Velocity snapshots at the beginning of the assimilation window ( $t'_1$ ) in the plane  $z = 1.31D$ . From left to right: streamwise, lateral, and spanwise fields. From top to bottom:  $Obs_{true}$ ,  $Obs_{inter}$ ,  $An_{case} (c)$ ,  $Obs_{rec}$  and  $An_{case} (d)$

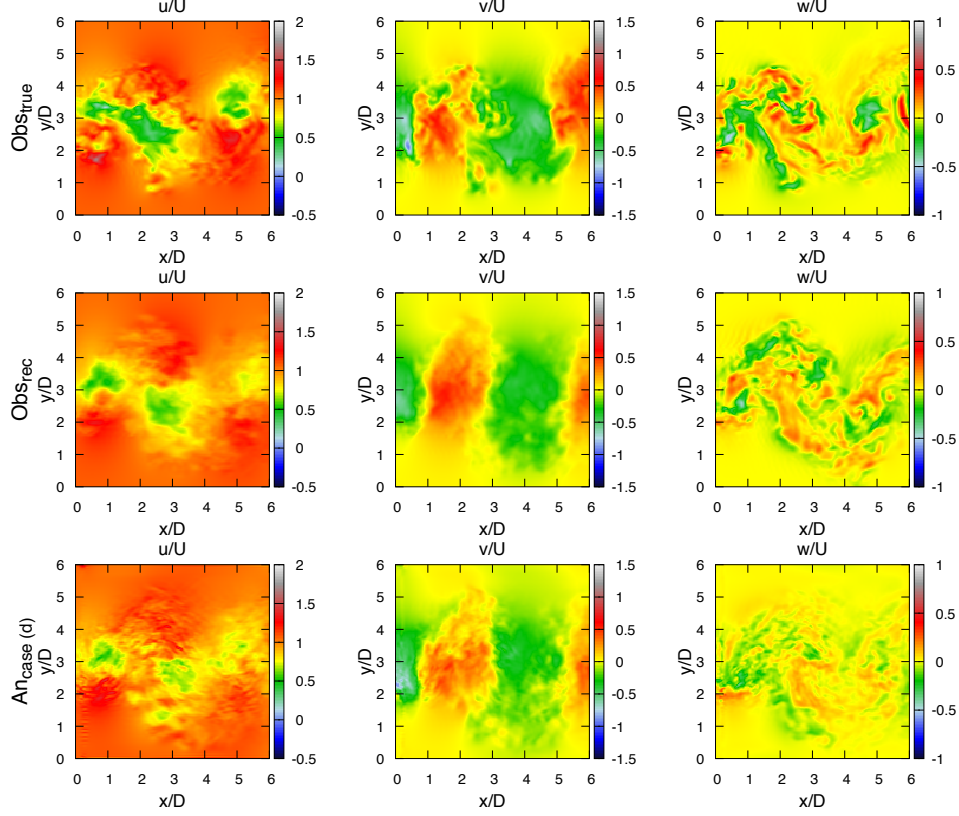


Figure 13: Velocity snapshots at the end of the assimilation window ( $t'_2$ ) in the plane  $z = 1.31D$ . From left to right: streamwise, lateral, and spanwise fields. From top to bottom:  $Obs_{true}$ ,  $Obs_{rec}$ , and  $An_{case} (c)$

#### 540 4.4.3. Analysis 3 - Background covariance

The use of an accurate, well-defined background covariance matrix  $\mathbf{B}$  is expected to provide significant improvements to the efficiency of the algorithm with faster convergence. However, the construction of the  $\mathbf{B}^{-1}$  matrix is usually cumbersome, requiring extensive computations and/or memory due to its  
545 considerable size. In this section, we use an innovative method, assisted by the SO algorithm, for estimating this matrix using multiple reconstructions.

Consider the fully synthetic case with 3D observations using SO reconstructed background initial condition. The data-collection step is run for a

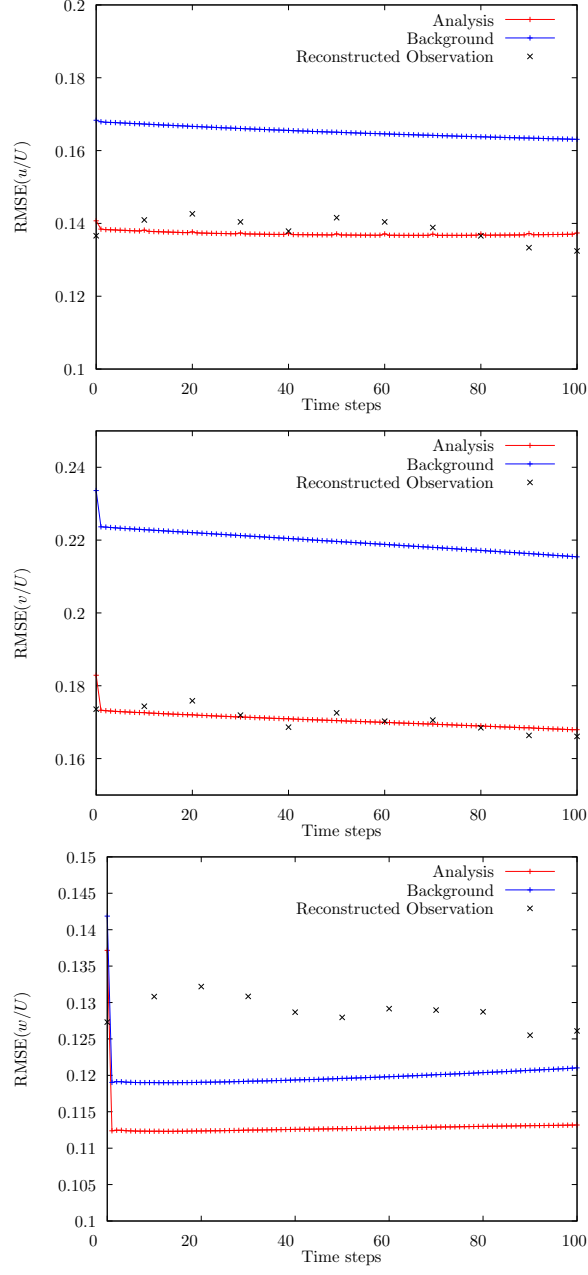


Figure 14: Evolution of the RMSE along time of the three velocity components between the true observations and the assimilation components, namely background, observation, and analysis for case (d).



long period producing 4000 snapshots with each snapshot spaced 50 time steps apart. The 2D3C cross-plane data is extracted from the 4000 snapshots for use with the SO algorithm. Instead of using all the 4000 snapshots for one single reconstruction, we use a sliding window for the number of OP snapshots used to create multiple reconstructions i.e. we use the first 400 OP snapshots for reconstruction #1, 200-600 for #2, 400-800 for #3, and so on giving us 19 reconstructed 3D velocity fields at one instant of time  $t'_1$ . Removing the mean and decomposing the set of reconstructed fields using singular value decomposition (SVD) gives an estimate for the background covariance matrix through the velocity fluctuations ( $\mathbf{u}'$ ) as,

$$\mathbf{u}' = USV^T, \quad (33)$$

where  $U$  contains the left singular vectors as columns,  $V^T$  contains the right singular vectors as rows, and  $S$  is a diagonal matrix composed of the singular values in decreasing order of magnitude. The background covariance matrix and its inverse can then be defined as,

$$\mathbf{B} = \mathbf{u}' \mathbf{u}'^T = (USV^T)(USV^T)^T = US^2U^T, \quad (34)$$

$$\mathbf{B}^{-1} = (US^2U^T)^{-1} = US^{-2}U^T, \quad (35)$$

$$\mathbf{B}^{-\frac{1}{2}} = US^{-1}U^T. \quad (36)$$

With the computed  $\mathbf{B}^{-\frac{1}{2}}$ , the components of the cost function and its gradient with respect to the background can be modified as,

$$J(\boldsymbol{\eta}) = \frac{1}{2} \|\boldsymbol{\mathcal{X}}_0^b - \boldsymbol{\mathcal{X}}_0\|_{\mathbf{B}^{-1}}^2 = \frac{1}{2} (\|\boldsymbol{\mathcal{X}}_0^b - \boldsymbol{\mathcal{X}}_0\|_{\mathbf{B}^{-\frac{1}{2}}} (\mathbf{B}^{-\frac{1}{2}})^T \|\boldsymbol{\mathcal{X}}_0^b - \boldsymbol{\mathcal{X}}_0\|^T), \quad (37)$$

$$\frac{\partial J}{\partial \boldsymbol{\eta}} = (\delta \boldsymbol{\mathcal{X}}_0 \mathbf{B}^{-\frac{1}{2}}) ((\mathbf{B}^{-\frac{1}{2}})^T). \quad (38)$$

Such an evaluation takes into account the effect that a change in velocity at one point has on other points in a neighbourhood through the inverse of the

$\mathbf{B}$  matrix. This should result in faster convergence due to a distributed optimisation procedure where convergence at each mesh-point assists in obtaining  
555 a better estimate of the field at other points with respect to the background condition.

This is studied by performing an assimilation run (case (e)) with identical parameters to case (b). The difference between the two cases lies in the definition of the  $\mathbf{B}^{-1}$  matrix which was set to identity in case (b) but is estimated in case (e). The cost functional and its gradient evolution for the two  
560 cases are shown in figure 15. A significantly faster convergence is obtained with case (e) (26 inner loop iterations) requiring only half the iterations of case (b) (58 inner loop iterations). The final cost is marginally higher in this case due to the increased weighting of the background error caused by the fully defined  
565 background covariance matrix. The gradient of the cost function for the initial set of iterations are identical for both cases but as the optimal trajectory deviates further from the background, the covariance matrix plays a role and thus, the two gradient curves deviate from each other. These characteristics suggest that a good estimate of the background covariance matrix provides a significant  
570 computational cost reduction by improving the efficiency of the optimisation algorithm.

The optimal analysis provided by the fully-resolved  $\mathbf{B}$  matrix case is shown in figure 16 at time  $t'_1$ . The corresponding analysis for case (b) is reproduced here for easy comparison. We can see that both analysis trajectories are comparable and match well with the reference. The RMSE evolution, shown in  
575 figure 17, highlights the slight differences between the two cases. The assimilation algorithm improves on the background condition with either covariance matrix, however, the analysis from case (b) is of lower error than case (e). This discrepancy, despite better information being provided through the background  
580 covariance matrix, could be due to a lack of detailed information on the observations e.g. lack of a well-defined observation covariance matrix. In the authors opinion, the significant reduction in computation cost obtained with a well-defined covariance off-sets the loss of accuracy in the analysis. In addition,

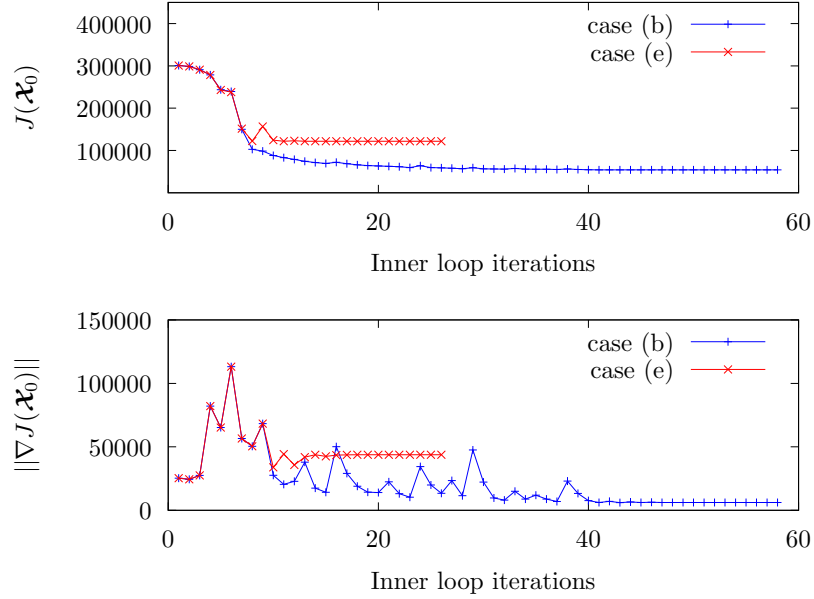


Figure 15: Evolution of the cost function  $J(\mathbf{x}_0)$  and its gradient  $\|\nabla J(\mathbf{x}_0)\|$  for the assimilation as a function of inner loop iterations for cases (b) and (e).

this could be improved by estimating the observation covariance matrix using  
 585 a similar methodology and by weighting appropriately the various contributors  
 to the cost function.

#### 4.5. Sliding window optimisation

A well-known drawback of VDA is the inability to assimilation observations  
 over a long assimilation time-window. In meteorological applications, the tem-  
 590 poral range of the assimilation window is estimated as the inverse of the first  
 Lyapunov exponent. This indicates the time-period within which a reliable fore-  
 cast can be made. A time-window larger than this estimate could result in the  
 unstable modes of the dynamics diverging quickly from the observations. This  
 limitation is why weather forecasting is restricted to a maximum prediction of  
 595 ten-days. As we shift focus to turbulent fluid flows, the time-domain associated  
 with the much finer scales of motion is significantly smaller. In our 4D-Var

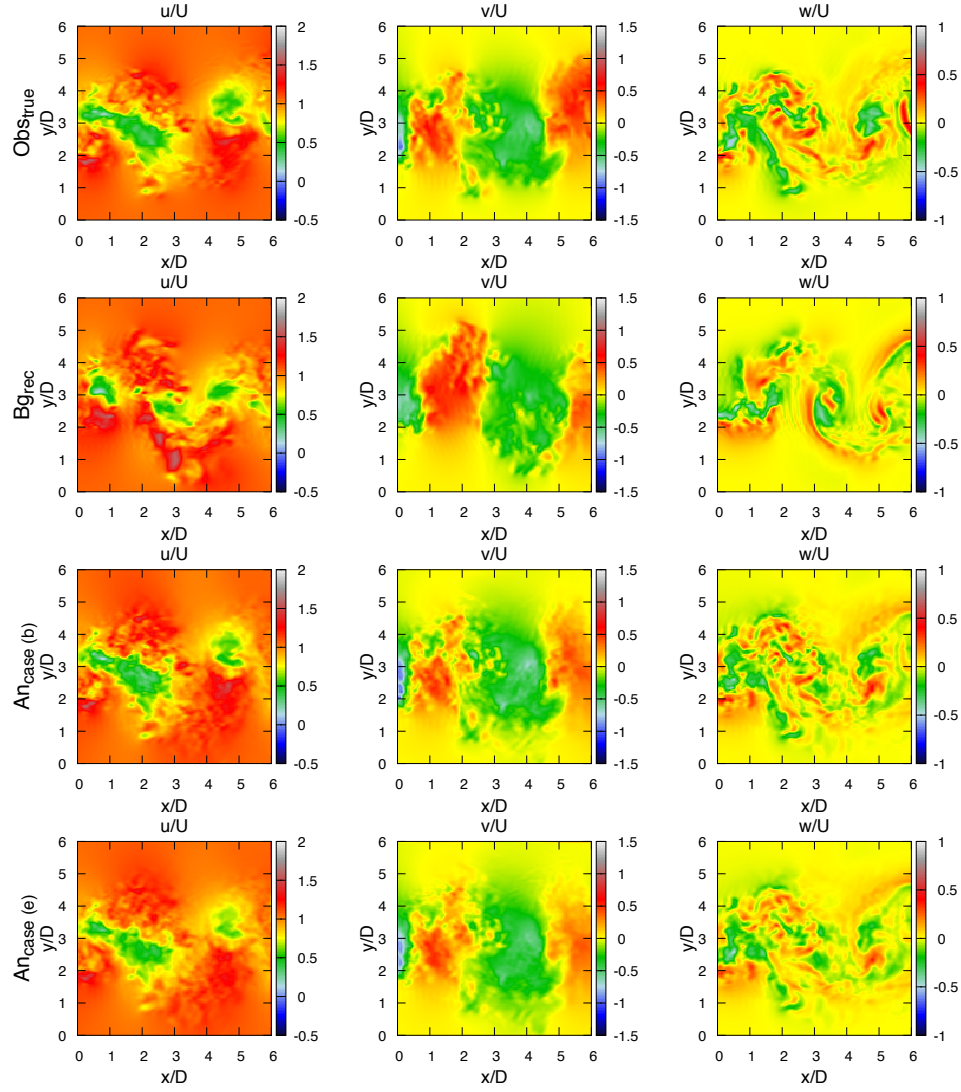


Figure 16: Velocity snapshots at the beginning of the assimilation window ( $t'_1$ ) in the plane  $z = 1.31D$ . From left to right: streamwise, lateral, and spanwise fields. From top to bottom:  $Ob_{true}$ ,  $Bg_{rec}$ ,  $An_{case} (b)$ , and  $An_{case} (e)$

algorithm, we restrict ourselves to only 100 time-steps for the assimilation window. This value has been empirically set. Estimation of the first Lyapunov exponent could lead to optimal size. However, such an estimation is very time consuming. This limitation is also inherent to SDA algorithms which requires

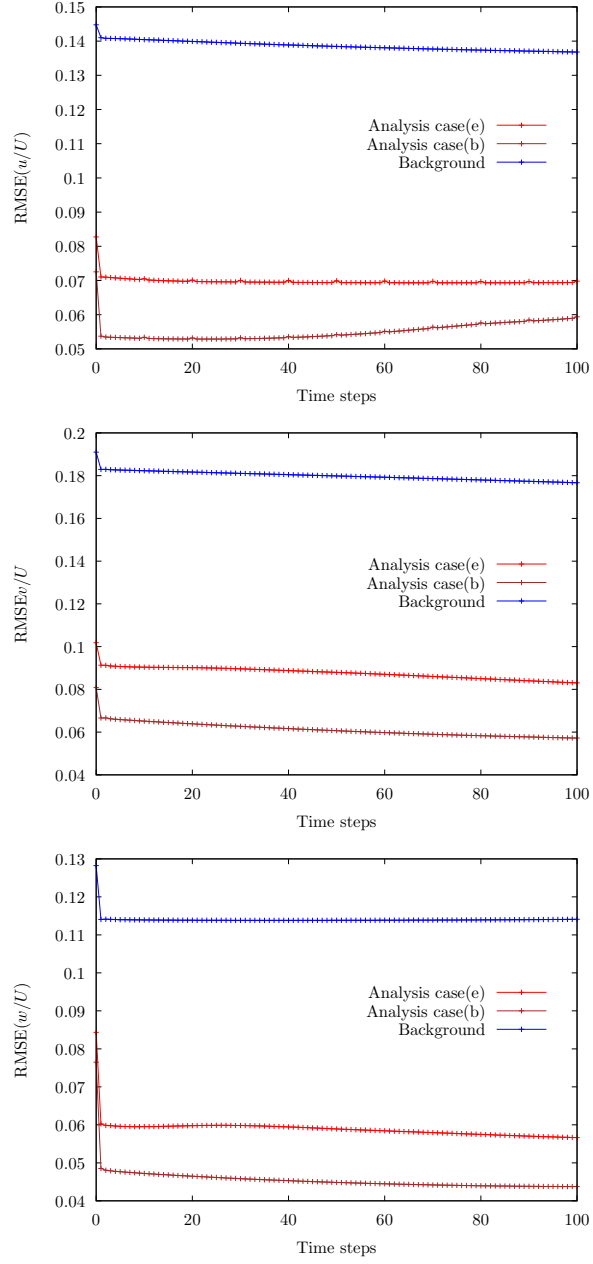


Figure 17: Evolution of the RMSE along time of the three velocity components between the true observations and the assimilation components, namely background, observation, and analysis for case (d).

larger ensembles for larger time-domains with increased observations leading to computational and memory difficulties.

In VDA, an innovative way to extend the time-period of assimilation is to use the concept of sliding windows [15, 16]. In this methodology, the 4D-Var  
605 algorithm is run with a given background condition for the short, reliable, fixed time-window (100 time-steps in this work) to obtain an optimal analysis trajectory. Depending on the choice of overlap (say 50%) for the sliding window, the analysis state at the corresponding time (at  $t = 50$  in our case) is chosen as the background condition for the next assimilation. This second assimilation  
610 begins at the overlap time (i.e. initial time,  $t_i = 50$ ) and observations are assimilated over the fixed time-window (thus, final time,  $t_f = 150$ ). With this second assimilation, an addition period of observations are incorporated into the algorithm while respecting the temporal window-size limitation. Multiple sliding window assimilations can then be performed to account for observations over  
615 a long time-period over which a single assimilation with the 4D-Var algorithm would diverge. A long time-period also ensures that converged statistics can be obtained for the flow which would not be possible within a single assimilation window. However, the application of sliding window assimilation increases significantly the computational cost as multiple assimilation runs need to be  
620 performed.

For wake flow around a circular cylinder at  $Re\ 3900$ , statistical convergence requires numerous vortex shedding cycles. A study by [34] suggested that a minimum of 50 cycles were necessary to achieve statistical convergence. This, with current computational limitations, is difficult to achieve with the 4D-Var  
625 algorithm requiring, by extrapolation, roughly one year of computations on a local grid computer.

In this section, we have performed the sliding window approach for one vortex shedding cycle, as a proof of concept, to show its capabilities for long term VDA. Three runs are performed: first with the true background and true observations  
630 ( $DA_{ideal}$ ), second with a reconstructed background and true observations ( $DA_{bg}$ ), and the third with reconstructed background and reconstructed

observations ( $DA_{rec}$ ). The velocity contours at the end of the final sliding window, corresponding to the 1700th time-step, is shown for the three cases along with the true and reconstructed observations at this instance in figure 18. With true observations, the assimilation, despite the background condition, captures the flow field accurately with respect to the observations. For  $DA_{rec}$ , the velocity contours appears to be at an intermediate state between the true observations and the reconstructed observations.

The lateral profiles of statistical quantities at three streamwise locations ( $X = 0.5D; 1D; 2D$  in the assimilation domain) are presented in figures 19-20 - the values have been translated for concise representation. Two additional direct simulations are run in the assimilation domain for one vortex shedding with the true background ( $Bg_{true}$ ) and the reconstructed background ( $Bg_{rec}$ ) to compared with the DA results. The profiles are matched with the DNS reference from [8].

All simulations match well with the reference for the mean streamwise profiles. The use of the sliding window provides additional time-steps for statistical averaging. Thus, the DA profiles are smoother and more converged than the direct profiles. The use of the averaged SO observations provides less turbulent, smooth flow fields. This leads to a smoother profile for  $DA_{rec}$  as compared to the other cases. The mean spanwise profile suggests that one vortex shedding is clearly not enough for statistical convergence for this quantity. It is interesting to note that when the observations provided for DA are turbulent, as is the case for  $DA_{ideal}$  and  $DA_{bg}$ , the convergence or smoothness of the profiles are reduced as compared  $DA_{rec}$ . The use of the averaging SO observations leads to significantly smoother profiles.

This does have an associated disadvantage with respect to the turbulent fluctuation profiles in figure 20. A clear under prediction of statistics is observed for  $DA_{rec}$  - a result of the smooth observations used. However, even in the fluctuation statistics, the  $DA_{rec}$  has the most converged statistics that matches best, in profile, with the reference albeit with lower magnitude. These results are encouraging towards the capability of 4D-Var to extend to larger

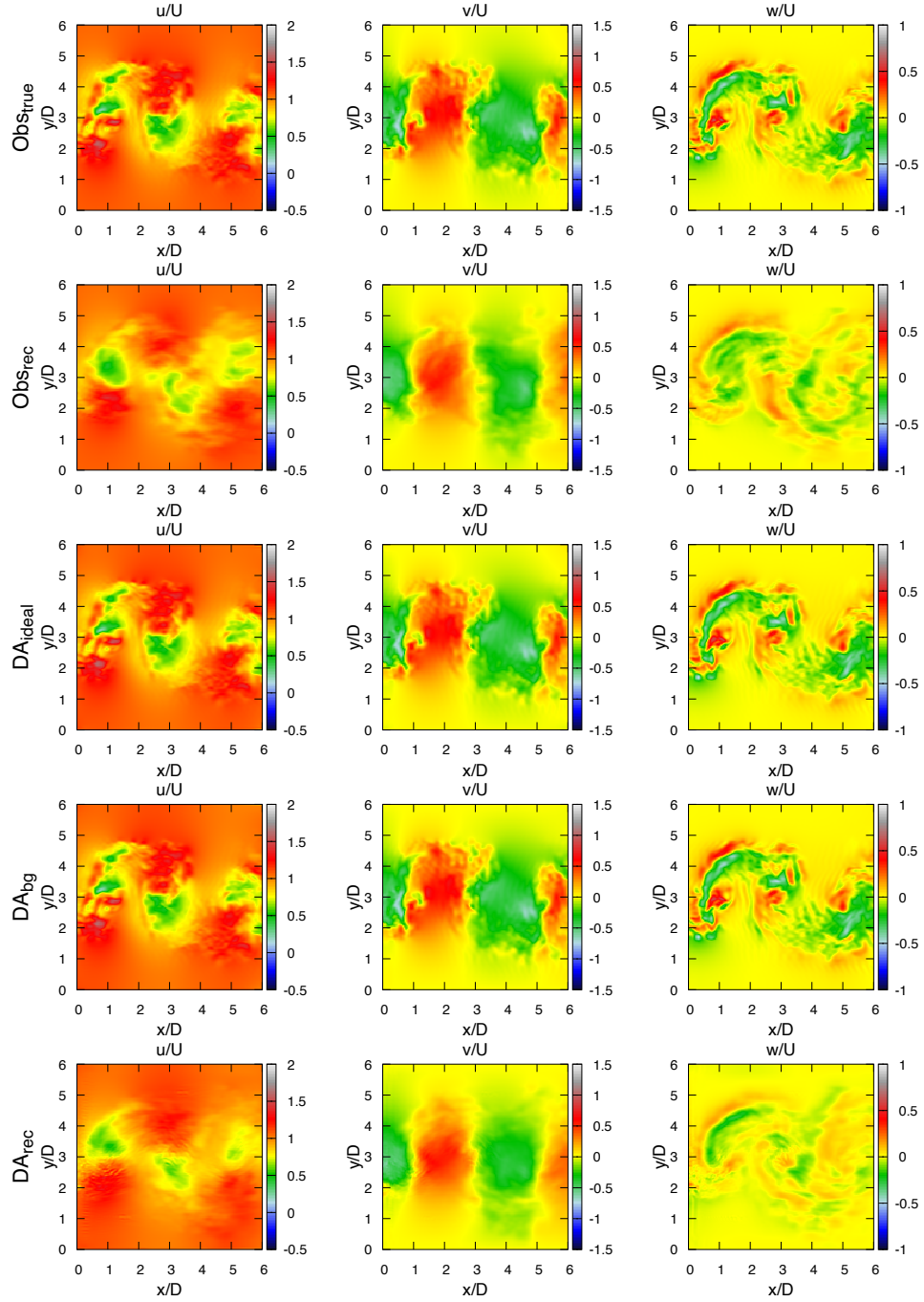
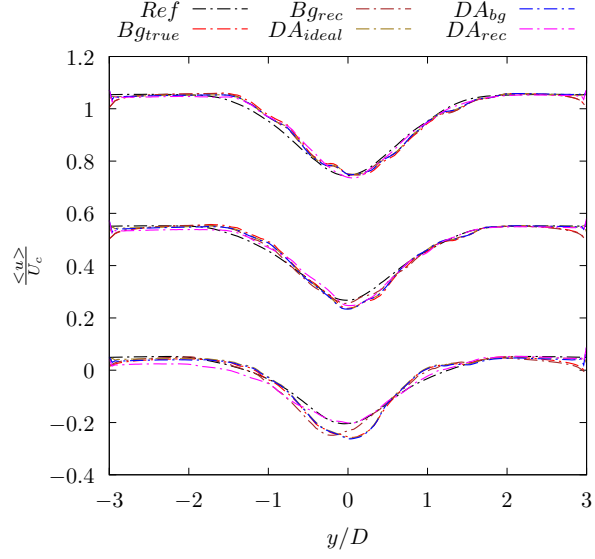
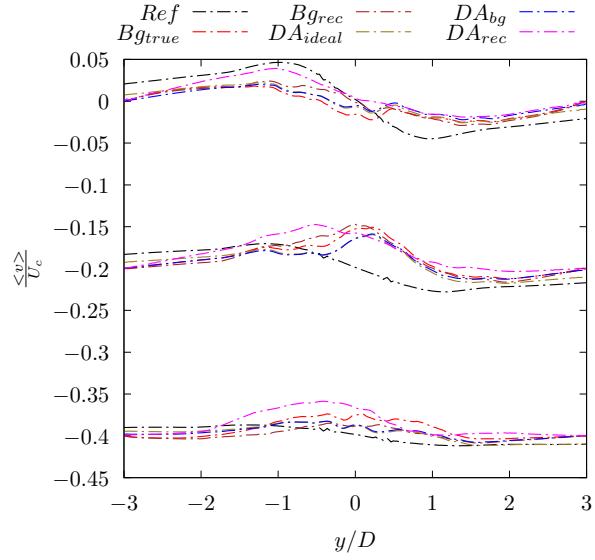


Figure 18: Velocity snapshots at the end of the final sliding window ( $t'_f = 1700$ ) in the plane  $z = 1.31D$ . From left to right: streamwise, lateral, and spanwise fields. From top to bottom:  $Obs_{true}$ ,  $Obs_{rec}$ , Analysis for  $DA_{ideal}$ ,  $DA_{bg}$  and  $DA_{rec}$  sliding window cases.





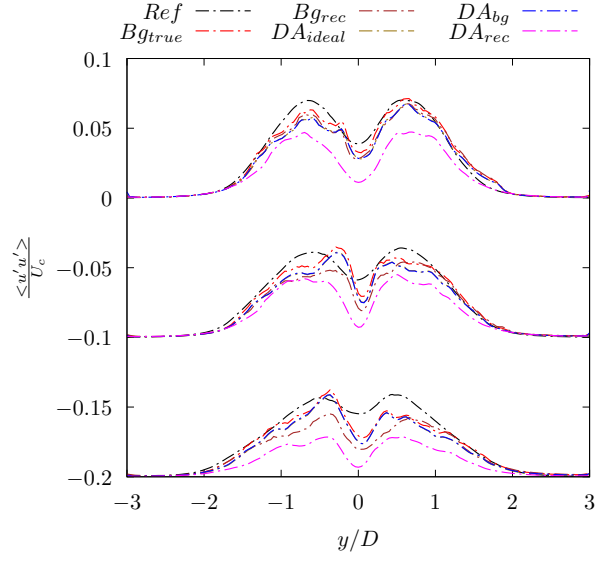
(a)  $\langle u \rangle$



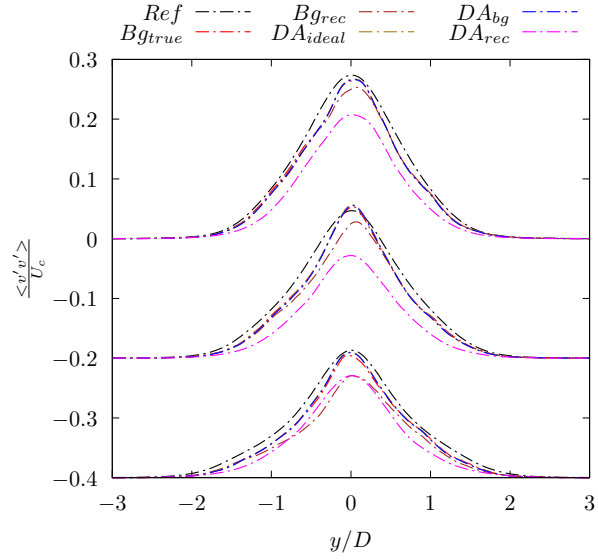
(b)  $\langle v \rangle$

Figure 19: Mean streamwise (a) and lateral (b) velocity profile along  $y$ , averaged along the spanwise ( $z$ ) direction.

assimilation time-domain with the help of sliding windows. It must be noted that the associated computational cost and time for performing sliding window



(a)  $\langle u'u' \rangle$



(b)  $\langle v'v' \rangle$

Figure 20: Fluctuating streamwise (a) and lateral (b) velocity profile along  $y$ , averaged along the spanwise ( $z$ ) direction.

665 assimilation needs to be considered.

## 5. Error model optimisation

By introducing the error model coefficient ( $C_{sp}$  in eq. (32)) as a control parameter ( $\vartheta$ ) in the variational assimilation algorithm, it can be optimised along with the initial velocity field maps. Estimation of an error model coefficient within a variational assimilation algorithm in 3D is a relatively new concept. To the extent of the authors' knowledge, this is the first attempt at analysing the capability of a VDA algorithm for estimating an error model coefficient for a turbulent flow. As explained in §2, this strategy provides a compromise solution between a strong assimilation constraint (case explored in §4) and a weak-constraint assimilation.

An initial estimate (equivalent to the background condition) for the coefficient is provided using eq. (32) - for a uniform mesh, this results in a constant coefficient estimate in time and space. Let us note that this value corresponds to the value used for the reference simulation (but with a stretched mesh and known boundary conditions). The optimised coefficient is enforced to be constant in time but allowed to vary in space. A penalty term is considered (see cost function eq. (39) below) on the coefficient to ensure it does not vary far from the background value provided. This is important for multiple reasons:

- The coefficient defines the amount of dissipation brought in by the model and the stability of the flow is predicated on this;
- The contribution to the cost function of the coefficient is only through the deviation from the initial estimate provided and this is multiple orders of magnitude smaller than the observation error. Thus, the algorithm tends to modify freely the coefficient in order to reduce the cost function in lieu of the initial/inlet condition.

The cost function including the additional control on the coefficient is given as,

$$J(\boldsymbol{\eta}, \vartheta) = \frac{1}{2} \|\boldsymbol{\eta}\|_{\mathbf{B}^{-1}}^2 + \frac{1}{2} \|\vartheta\|_{\mathbf{B}^c}^2 + \frac{1}{2} \int_{t_0}^{t_f} \|\mathbb{H}(\boldsymbol{\mathcal{X}}_t) - \boldsymbol{\mathcal{Y}}(t)\|_{\mathbf{R}^{-1}}^2 dt, \quad (39)$$

where  $\vartheta = C_0 - C_b$  is the difference between the coefficient estimate and the background value given by eq. (32), and  $\mathbf{B}_c^{-1}$  is the corresponding covariance which is set to Identity. The gradient, using the adjoint approach, is defined as,

$$\frac{\partial J}{\partial \boldsymbol{\eta}} = -\boldsymbol{\lambda}_{t_0} + \mathbf{B}^{-1} \delta \mathcal{X}_0, \quad (40)$$

$$\frac{\partial J}{\partial \vartheta} = -\boldsymbol{\lambda}_{t_0} + \mathbf{B}_c^{-1} \vartheta + (\partial_{\vartheta} \mathbb{M})^* \boldsymbol{\lambda}. \quad (41)$$

where  $(\partial_{\vartheta} \mathbb{M})^*$  refers to the adjoint dynamic model with respect to the coefficient formulated using TAPENADE, the AD tool. It is interesting to note that due to the linear nature of the coefficient in the dynamical model (see eq. (31)), the tangent dynamical model with respect to the coefficient is the model itself without the coefficient.

An assimilation study (case (f)) is performed with reconstructed observations and a reconstructed background condition emulating experimental measurements with a fully-defined inverse of the background covariance matrix. **This case corresponds thus to the most finalised assimilation strategy with experimentally realistic measurements and an error model calibrated from these data.** The coefficient is allowed to vary in space while it is assumed constant in time. The resultant analysis trajectory is similar to that of case (d) and is not shown here to avoid repetition. Figure 21 presents the 2D contour map of the initial and optimised model coefficient. The optimised coefficient varies in space and is in general stronger than the initial condition obtained from the model equation implying higher dissipation in such regions. These regions of higher value matches well with the locations of strong vorticity of the flow (see figure 22). Such regions of high turbulence imply active sub-grid scales and thus require a stronger contribution of the model characterised by the larger coefficient value.

The validity of the optimised coefficient is supported by the RMSE evolution in figure 23 where two identical cases with and without coefficient optimisation are compared. By optimising the coefficient, a lower RMSE is obtained for all

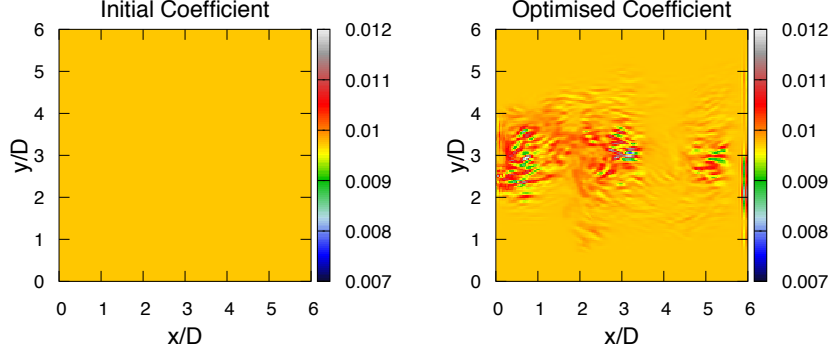


Figure 21: LES model coefficient contour map in the streamwise plane  $z = 1.31D$  for case (f). From left to right: background, and analysis.

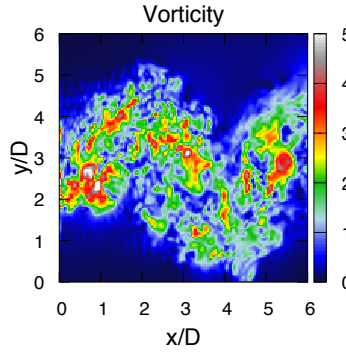


Figure 22: Instantaneous flow vorticity in the streamwise plane  $z = 1.31D$  calculated from the true observations.

three velocity components than with a fixed coefficient despite both requiring  
715 roughly the same number of iterations. In addition, this error gap between the  
two cases appears to widen as we evolve along time with improved prediction  
with the optimised coefficient. This suggests that the optimised coefficient is a  
better representation of the dynamical evolution of the flow taking into account  
the small-scale contributions. Thus, an evolution in time beyond the assimila-  
720 tion window should further improve the prediction than with a non-optimised  
coefficient. A sliding window algorithm with coefficient optimisation can easily  
be envisioned, however, it has not been attempted due to the high computa-

tional cost requirements. These preliminary results are very interesting and shows the capability of the proposed assimilation scheme to go towards error  
725 model parametrisation, a concept that has been at the forefront of research over many decades [3, 4, 21]. Let us stress again that these results are obtained here without any modelling of the obstacle. Only a symmetry of the obstacle is exploited in the reconstruction method. This technique provides rough volumetric observations and is associated with a covariance matrix that strongly penalises  
730 observations far from the observed planes. As a consequence, this technique could probably also be used for non-symmetric obstacles.

## 6. Conclusions

This article presents a new variational data assimilation approach, termed as 4D-Var, building on the work of Gronsksis et al. [20] for assimilation of 3D,  
735 unsteady, incompressible turbulent flows. The LU turbulence model of Mémin [29] was coupled with VDA principles to take into account errors in the dynamics of the assimilated model. Such a strategy enables us to consider a variational assimilation strategy which is a compromise between a strong constraint assimilation without error, and a weakly constrained assimilation with  
740 a non-informative Gaussian error model.

The 4D-Var algorithm has been successfully applied to turbulent wake behind a circular cylinder at a Reynolds number of 3900 in the transitional regime of cylinder wake flow. A parametric study was performed on three crucial inputs for the 4D-Var algorithm, i.e. the background condition, the observation  
745 data-sets, and the background covariance matrix to conclude the following: A physically meaningful background improved the accuracy of the assimilation at lower cost than an inaccurate estimate of the background. The quality of the observation data-set was directly correlated to algorithm stability. Analysis trajectories incorporating interpolated observations were seen to be unstable when  
750 non-linearly evolved in time. Observations reconstructed using the SO methodology were better suited giving stable analysis velocity fields. A fully-defined

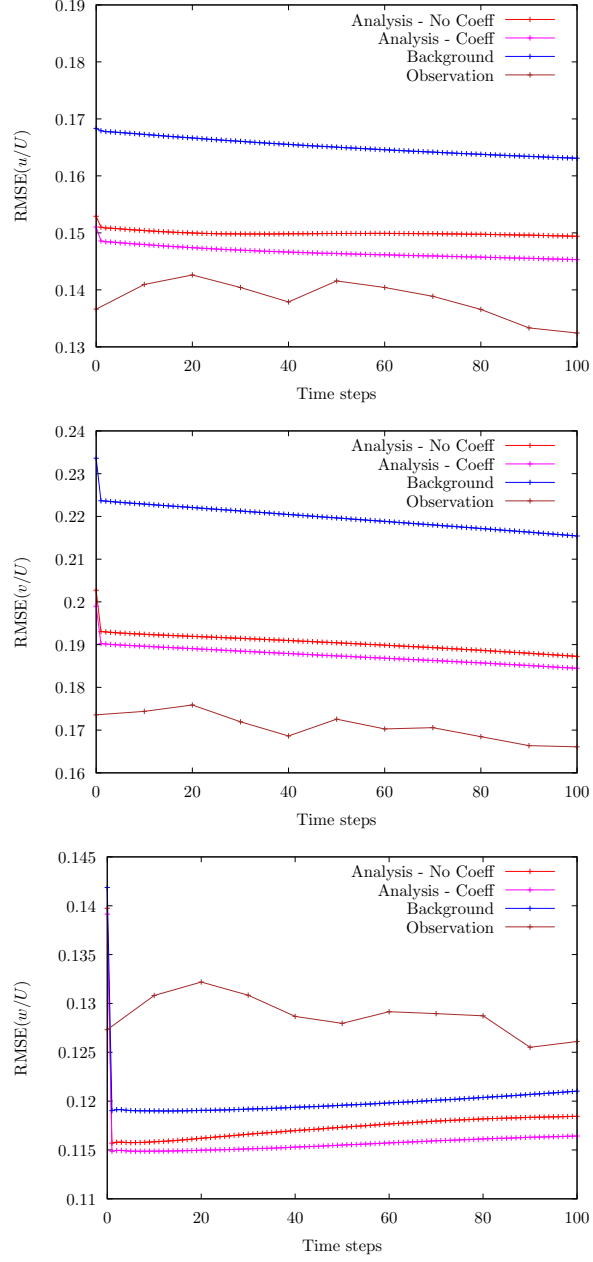


Figure 23: Evolution of the RMSE along time of the three velocity components between the true observations and the assimilation components, namely background, observation, and analysis for assimilation with and without coefficient optimisation.

inverse of the background covariance matrix provides faster convergence requiring only  $\sim 50\%$  of the iterations but with an associated loss of accuracy -  $\sim 15\text{-}20\%$  at the beginning of the assimilation window in comparison with results  
755 obtained for an inverse background covariance matrix set to Identity.

An interesting avenue of research opened by combining an error model, representing turbulent small-scale flow structures, with an optimisation approach is the ability to tune model contribution predicated on observations. For the LU model, this tuning is introduced via the model coefficient,  $C_{sp}$ , which is im-  
760 plemented as a control parameter in the 4D-Var algorithm and optimised along with the initial condition. The tuned coefficient was observed to be stronger in regions corresponding to high vorticity, i.e. regions of high turbulence and thus stronger sub-grid scale activity, i.e. larger model error. The RMSE for the optimal velocity prediction with the tuned coefficient is lower than when the  
765 model coefficient is not optimised. This proposed assimilation strategy coupled with the LU modelling allows us, for the first time to the authors knowledge, to consider the reconstruction of a 3D turbulent flow without modelling explicitly the obstacle geometry together with an explicit control of the error model. In this work, we have shown that parameter estimation is possible with VDA  
770 and provides good results despite the requirement of an additional adjoint with respect to the parameter.

Future work would focus on the application of the algorithm to experimental data-sets such as cross-plane PIV measurements or volumetric PIV measurements. The results presented here with reconstructed observations emulating  
775 experimental data were encouraging towards assimilation of such experimental observations. The control of boundary conditions as parameters in the 4D-Var algorithm is another interesting avenue of research that needs exploration. With the current algorithm, small discontinuities can be observed at the outlet condition for certain parameters, for example with the optimised model coefficient.  
780 By implementing the outlet condition as a control parameters, a better estimate could probably be obtained at the outlet.



## References

## References

- [1] Artana, G., Cammilleri, A., Carlier, J., Mémin, E., 2012. Strong and weak  
785 constraint variational assimilations for reduced order fluid flow modeling.  
J. Comput. Phys. 231 (8), 3264–3288.
- [2] Bergthórsson, P., Döös, B. R., 1955. Numerical Weather Map Analysis.  
Tellus 7 (3), 329–340.
- [3] Cardinali, C., Žagar, N., Radnoti, G., Buizza, R., Sep. 2014. Representing  
790 model error in ensemble data assimilation. Nonlinear Processes in Geo-  
physics 21 (5), 971–985.
- [4] Carrassi, A., Vannitsem, S., Nicolis, C., Jul. 2008. Model error and sequen-  
tial data assimilation: A deterministic formulation. Quarterly Journal of  
the Royal Meteorological Society 134 (634), 1297–1313.
- [5] Chandramouli, P., 2018. Turbulent complex flows reconstruction via data  
795 assimilation in large eddy models. Scientific, Université de Rennes 1,  
Rennes.
- [6] Chandramouli, P., Mémin, E., Chapron, B., Laizet, S., Heitz, D., ????  
Deciphering the role of small-scale inhomogeneity on flow structuration: a  
800 stochastic approach. Submitted to Science.
- [7] Chandramouli, P., Memin, E., Heitz, D., Fiabane, L., 2019. Fast 3d flow  
reconstructions from 2d cross-plane observations. Experiments in Fluids  
60, 30.
- [8] Chandramouli, P., Memin, E., Heitz, D., Laizet, S., 2018. Coarse large-eddy  
805 simulations in a transitional wake flow with flow models under location  
uncertainty. Comput. Fluids 168, 170–189.

- [9] Chapron, B., Derian, P., Mémin, E., Resseguier, V., 2018. Large scale flows under location uncertainty: a consistent stochastic framework. *Q. J. R. Meteorolog. Soc.* 144 (710), 251–260.
- 810 [10] Cressman, G. P., 1959. An operational objective analysis system. *Mon. Weather Rev.* 87 (10), 367–374.
- [11] D’adamo, J., Papadakis, N., Mémin, E., Artana, G., 2007. Variational assimilation of POD low-order dynamical systems. *J. Turbul.* 8, N9.
- [12] Elsinga, G. E., Scarano, F., Wieneke, B., van Oudheusden, B. W., 2006. 815 Tomographic particle image velocimetry. *Exp. Fluids* 41 (6), 933–947.
- [13] Evensen, G., 1994. Sequential data assimilation with a nonlinear quasi-geostrophic model using Monte Carlo methods to forecast error statistics. *J. Geophys. Res. Oceans* 99 (C5), 10143–10162.
- [14] Evensen, G., 2009. The ensemble Kalman filter for combined state and 820 parameter estimation. *IEEE Control Systems* 29 (3).
- [15] Fang, P., Bock, Y., 1998. Sliding window procedure for super near real-time continuous GPS water vapor estimation using predicted orbits. *Annales Geophysicae* 16 (Suppl. I).
- [16] Foster, J., Bevis, M., Businger, S., Jun. 2005. GPS Meteorology: Sliding- 825 Window Analysis\*. *Journal of Atmospheric and Oceanic Technology* 22 (6), 687–695.
- [17] Foures, D. P. G., Dovetta, N., Sipp, D., Schmid, P. J., 2014. A data-assimilation method for Reynolds-averaged Navier–Stokes-driven mean flow reconstruction. *J. Fluid Mech.* 759, 404–431.
- 830 [18] Gautier, R., Laizet, S., Lamballais, E., 2014. A DNS study of jet control with microjets using an immersed boundary method. *Int. J. Comput. Fluid Dyn.* 28 (6-10), 393–410.

- 835 [19] Gordon, N. J., Salmond, D. J., Smith, A. F. M., 1993. Novel approach to nonlinear/non-Gaussian Bayesian state estimation. IEE Proceedings F - Radar and Signal Processing 140 (2), 107.
- [20] Gronsksis, A., Heitz, D., Mémin, E., 2013. Inflow and initial conditions for direct numerical simulation based on adjoint data assimilation. J. Comput. Phys. 242, 480–497.
- 840 [21] Harlim, J., 2017. Model error in data assimilation. In: Nonlinear and Stochastic Climate Dynamics. Cambridge University Press.
- [22] Hascoët, L., Pascual, V., 2004. TAPENADE 2.1 user’s guide. Tech. rep.
- [23] Kadri Harouna, S., Mémin, E., 2017. Stochastic representation of the Reynolds transport theorem: revisiting large-scale modeling. Comput. Fluids 156, 456–469.
- 845 [24] Kim, J., Bodony, D., Freund, J., Jun. 2010. A High-Order, Overset-Mesh Algorithm for Adjoint-Based Optimization for Aeroacoustics Control. In: 16th AIAA/CEAS Aeroacoustics Conference. American Institute of Aeronautics and Astronautics, Stockholm, Sweden.
- 850 [25] Laizet, S., Lamballais, E., 2009. High-order compact schemes for incompressible flows: A simple and efficient method with quasi-spectral accuracy. J. Comput. Phys. 228 (16), 5989–6015.
- [26] Le Dimet, F.-X., Talagrand, O., 1986. Variational algorithms for analysis and assimilation of meteorological observations: theoretical aspects. Tellus A 38 (2), 97–110.
- 855 [27] Lions, J., 1971. Optimal control of systems governed by partial differential equations problèmes aux limites. Berlin: Springer, 407.
- [28] Meldi, M., Poux, A., 2017. A reduced order model based on Kalman filtering for sequential data assimilation of turbulent flows. J. Comput. Phys. 347, 207–234.

- 860 [29] Mémin, E., 2014. Fluid flow dynamics under location uncertainty. *Geophys. Astro. Fluid* 108 (2), 119–146.
- [30] Mons, V., Chassaing, J.-C., Gomez, T., Sagaut, P., 2016. Reconstruction of unsteady viscous flows using data assimilation schemes. *J. Comput. Phys.* 316, 255–280.
- 865 [31] Mons, V., Chassaing, J.-C., Sagaut, P., Jul. 2017. Optimal sensor placement for variational data assimilation of unsteady flows past a rotationally oscillating cylinder. *Journal of Fluid Mechanics* 823, 230–277.
- [32] Nocedal, J., 1980. Updating quasi-Newton matrices with limited storage. *Math. Comput.* 35 (151), 773–782.
- 870 [33] Papadakis, N., Mémin, E., Cuzol, A., Gengembre, N., 2010. Data assimilation with the weighted ensemble Kalman filter. *Tellus A* 62 (5), 673–697.
- [34] Parnaudeau, P., Carlier, J., Heitz, D., Lamballais, E., 2008. Experimental and numerical studies of the flow over a circular cylinder at Reynolds number 3900. *Phys. Fluids* 20 (8), 085101.
- 875 [35] Resseguier, V., Mémin, E., Chapron, B., 2017. Geophysical flows under location uncertainty, Part I Random transport and general models. *Geophys. Astro. Fluid* 111 (3), 149–176.
- [36] Resseguier, V., Mémin, E., Chapron, B., 2017. Geophysical flows under location uncertainty, Part II Quasi-geostrophy and efficient ensemble spreading. *Geophys. Astro. Fluid* 111 (3), 177–208.
- 880 [37] Resseguier, V., Mémin, E., Chapron, B., 2017. Geophysical flows under location uncertainty, Part III SQG and frontal dynamics under strong turbulence conditions. *Geophys. Astro. Fluid* 111 (3), 209–227.
- [38] Sasaki, Y., 1958. An Objective Analysis Based on the Variational Method. *J. Meteorolog. Soc. Jpn. Ser. II* 36 (3), 77–88.
- 885

- [39] Sasaki, Y., 1970. Some basic formalisms in numerical variational analysis. Mon. Weather Rev. 98 (12), 875–883.
- [40] Suzuki, T., Ji, H., Yamamoto, F., Jul. 2010. Instability waves in a low-Reynolds-number planar jet investigated with hybrid simulation combining particle tracking velocimetry and direct numerical simulation. Journal of Fluid Mechanics 655, 344–379.
- [41] Tissot, G., Cordier, L., Benard, N., Noack, B. R., 2014. Model reduction using dynamic mode decomposition. C. R. Mécanique 342 (6-7), 410–416.
- [42] Yang, Y., Mémin, E., 2017. High-resolution data assimilation through stochastic subgrid tensor and parameter estimation from 4denvar. Tellus A 69, 1–24.
- [43] Yang, Y., Robinson, C., Heitz, D., Mémin, E., 2015. Enhanced ensemble-based 4dvar scheme for data assimilation. Comput. Fluids 115, 201–210.

## Appendix A. Interpolation method for $Obs_{inter}$

The interpolation method used for obtained  $Obs_{inter}$  in §4.4.2 is as follows,

$$w_1 = \exp(-(x - x_0)^2/(2.)) \quad (\text{A.1})$$

$$w_2 = \exp(-(z - (\frac{L_z}{2}))^2/(2.)) \quad (\text{A.2})$$

$$\mathbf{u}(x, y, z) = (\mathbf{u}(x_0, y, z) * w_1 + \mathbf{u}(x, y, z_0) * w_2)/(w_1 + w_2) \quad (\text{A.3})$$

$w_1$  defines the weight for the inlet plane velocity data while  $w_2$  defines the weight for the XY plane in the middle of the spanwise domain.

## Appendix B. Calculation of $R_{3D}^{-1}$ and $R_{PIV}^{-1}$

The observation covariance matrix  $R_{3D}^{-1}$  is implemented to be a function of space in order to account for boundary condition effects. A hyperbolic profile is used to reduce confidence in regions near the boundaries smoothly up to a

user-defined minimum value ( $\mathbf{R}_{min}^{-1}$ ). A user defined maximum ( $\mathbf{R}_{max}^{-1}$ ) value is enforced in the middle of the domain. In the streamwise direction, due to the availability of measurements on the inlet plane, confidence is reduced only near the outlet boundary. The algorithm for defining the observation covariance matrix  $\mathbf{R}_{3D}^{-1}$  for the reference observations is mathematically expressed as,

$$\mathbf{R}_{3D}^{-1}(x, y, z) = \frac{1}{2}(\tanh(-2.0(x - 0.9L_x)) + 1) \quad (\text{B.1})$$

$$\begin{aligned} \mathbf{R}_{3D}^{-1}(x, y, z) = \mathbf{R}_{3D}^{-1}(x, y, z) * \frac{1}{2}(\tanh(-2.0(y - \frac{L_y}{2} - 0.5L_y)) \\ - \tanh(-2.0(y - \frac{L_y}{2} + 0.5L_y))) \end{aligned} \quad (\text{B.2})$$

$$\begin{aligned} \mathbf{R}_{3D}^{-1}(x, y, z) = \mathbf{R}_{3D}^{-1}(x, y, z) * \frac{1}{2}(\tanh(-2.0(z - \frac{L_z}{2} - 0.5L_z)) \\ - \tanh(-2.0(z - \frac{L_z}{2} + 0.5L_z))) \end{aligned} \quad (\text{B.3})$$

$$\mathbf{R}_{3D}^{-1}(x, y, z) = \mathbf{R}_{3D}^{-1}(x, y, z) * (R_{max}^{-1} - R_{min}^{-1}) + R_{min}^{-1} \quad (\text{B.4})$$

The reconstructed or interpolated observations are not an exact representation of the reference field and thus, this needs to be reflected in the corresponding inverse of the observation covariance matrix ( $\mathbf{R}_{PIV}^{-1}$ ). Only the two observed planes command high confidence while the rest have minimal confidence defined up to a user defined minimum and maximum confidence ( $\mathbf{R}_{min}^{-1}$  and  $\mathbf{R}_{max}^{-1}$  respectively). Thus, maximum confidence is given to the points falling on these two planes with an exponential decrease in confidence away from the observed

planes. The covariance matrix is thus constructed as,

$$\mathbf{R}_{P_{IV}}^{-1}(x, y, z) = \max\left(\exp\left(-\frac{x^2}{0.05}\right), \exp\left(-\frac{(z - 0.5L_z)^2}{0.05}\right), R_{min}^{-1}\right) \quad (\text{B.5})$$

$$\mathbf{R}_{P_{IV}}^{-1}(x, y, z) = \mathbf{R}_{P_{IV}}^{-1}(x, y, z) * \exp\left(-\frac{(x - 0.9L_x)^2}{0.1}\right) \quad \forall x \geq 0.9L_x \quad (\text{B.6})$$

$$\mathbf{R}_{P_{IV}}^{-1}(x, y, z) = \mathbf{R}_{P_{IV}}^{-1}(x, y, z) * \exp\left(-\frac{(y - 0.1L_y)^2}{0.1}\right) \quad \forall y \leq 0.1L_y \quad (\text{B.7})$$

$$\mathbf{R}_{P_{IV}}^{-1}(x, y, z) = \mathbf{R}_{P_{IV}}^{-1}(x, y, z) * \exp\left(-\frac{(y - 0.9L_y)^2}{0.1}\right) \quad \forall y \geq 0.9L_y \quad (\text{B.8})$$

$$\mathbf{R}_{P_{IV}}^{-1}(x, y, z) = \mathbf{R}_{P_{IV}}^{-1}(x, y, z) * \exp\left(-\frac{(z - 0.1L_z)^2}{0.1}\right) \quad \forall z \leq 0.1L_z \quad (\text{B.9})$$

$$\mathbf{R}_{P_{IV}}^{-1}(x, y, z) = \mathbf{R}_{P_{IV}}^{-1}(x, y, z) * \exp\left(-\frac{(z - 0.9L_z)^2}{0.1}\right) \quad \forall z \geq 0.9L_z \quad (\text{B.10})$$

$$\mathbf{R}_{P_{IV}}^{-1}(x, y, z) = \max(\mathbf{R}_{P_{IV}}^{-1}(x, y, z), R_{min}^{-1}) * R_{max}^{-1} \quad (\text{B.11})$$

On the mid streamwise plane and the inlet plane strong confidence is given taking into account boundary effect at the edges. Along the transverse plane, a steep exponential slope is enforced to reduce covariance as we move away from the two planes of true observation.

905